



**HAL**  
open science

## Optical and photocatalytic properties of TiO<sub>2</sub>-Bi<sub>2</sub>O<sub>3</sub>-CuO supported on natural zeolite for removing Safranin-O dye from water and wastewater

Reguia Boudraa, Djahida Talantikite-Touati, Abdelhafid Souici, Atmane Djermoune, Amira Saidani, Karim Fendi, Abdeltif Amrane, Jean-Claude Bollinger, Hai Nguyen Tran, Amina Hadadi, et al.

### ► To cite this version:

Reguia Boudraa, Djahida Talantikite-Touati, Abdelhafid Souici, Atmane Djermoune, Amira Saidani, et al.. Optical and photocatalytic properties of TiO<sub>2</sub>-Bi<sub>2</sub>O<sub>3</sub>-CuO supported on natural zeolite for removing Safranin-O dye from water and wastewater. *Journal of Photochemistry and Photobiology A: Chemistry*, 2023, 443, pp.114845. 10.1016/j.jphotochem.2023.114845 . hal-04221242

**HAL Id: hal-04221242**

**<https://hal.science/hal-04221242v1>**

Submitted on 3 Sep 2024

**HAL** is a multi-disciplinary open access archive for the deposit and dissemination of scientific research documents, whether they are published or not. The documents may come from teaching and research institutions in France or abroad, or from public or private research centers.

L'archive ouverte pluridisciplinaire **HAL**, est destinée au dépôt et à la diffusion de documents scientifiques de niveau recherche, publiés ou non, émanant des établissements d'enseignement et de recherche français ou étrangers, des laboratoires publics ou privés.

# Optical and photocatalytic properties of TiO<sub>2</sub>–Bi<sub>2</sub>O<sub>3</sub>–CuO supported on natural zeolite for removing Safranin-O dye from water and wastewater

Reguia Boudraa<sup>1</sup>, Djahida Talantikite-Touati<sup>2</sup>, Abdelhafid Souici<sup>3</sup>, Atmane Djermoune<sup>4</sup>, Amira Saidani<sup>5</sup>, Karim Fendi<sup>5</sup>, Abdeltif Amrane<sup>6</sup>, Jean-Claude Bollinger<sup>7</sup>, Hai Nguyen Tran<sup>8,9</sup>, Amina Hadadi<sup>10</sup> Lotfi Mouni<sup>10,\*</sup>

<sup>1</sup> Laboratory of Materials and Durable Development (M2D), University Bouira, 1000, Bouira, Algeria

<sup>2</sup> Laboratoire de Génie de l'Environnement, Faculté de Technologie, Université de Bejaia, 06000 Bejaia, Algérie

<sup>3</sup> Laboratoire de physico-chimie des matériaux et catalyse, Faculté des Sciences Exactes Université de Bejaia, Bejaia 06000, Algeria

<sup>4</sup> Centre de Recherche Scientifique et Technique en Analyses Physico-chimiques (CRAPC), Bou-Ismaïl 42004, Tipaza, Algeria

<sup>5</sup> Laboratory Processes for Materials, Energy, Water and Environment. Faculty of Science and Technology, University of Bouira, 10000 Bouira, Algeria

<sup>6</sup> Université de Rennes, Ecole Nationale Supérieure de Chimie de Rennes, CNRS, ISCR – UMR6226, 35000 Rennes, France

<sup>7</sup> Laboratoire E2Lim (Eau Environnement Limoges), Université de Limoges, 123 Avenue Albert Thomas, 87060 Limoges, France

<sup>8</sup> Center for Energy and Environmental Materials, Institute of Fundamental and Applied Sciences, Duy Tan University, Ho Chi Minh, 700000, Vietnam

<sup>9</sup> Faculty of Environmental and Chemical Engineering, Duy Tan University, Da Nang, 550000, Vietnam

<sup>10</sup> Laboratoire de Gestion et Valorisation des Ressources Naturelles et Assurance Qualité. Faculté SNVST, Université , Bouira 10000, Algeria

\*Corresponding author: E-mail: [l.mouni@univ-bouira.dz](mailto:l.mouni@univ-bouira.dz), Tel.: +213-784-42-62-28

## Abstract

A series of *n-p* heterojunction catalysts (TiO<sub>2</sub>–Bi<sub>2</sub>O<sub>3</sub>–CuO) were synthesized by the ceramic method. X-ray diffraction, scanning electron microscopy coupled with energy dispersive X-ray, Fourier transform infrared spectroscopy (FTIR), UV-visible spectroscopy, and photoluminescence were used for the characterization of the synthesized materials. The optical optimization demonstrated that the solid solution TiO<sub>2</sub>–0.2Bi<sub>2</sub>O<sub>3</sub>–0.25CuO exhibited the best optical property. This catalyst supported on natural zeolite under ultrasonic waves improved notably the adsorption-photodegradation capacity of the resultant material. The impact of the *n-p* junction supported on zeolite on the photodegradation of a polluting solution showed excellent results for the degradation of cationic dye with removal efficiency reaching 94.1% and 80.23% under sunlight for Safranin-O dye in distilled water and in wastewater from a local textile dyeing plant.

---

**Keywords:** TiO<sub>2</sub>; Bi<sub>2</sub>O<sub>3</sub>; CuO; Cationic dye removal; Heterojunction; Photocatalysis; Wastewater treatment.

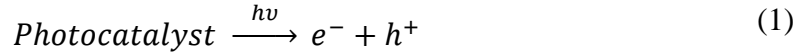
## 1. Introduction

Organic pollutants (i.e., hydrocarbons, pesticides, dioxins, dyes, chlorinated solvents, and drugs) are chemical molecules resulting from human activities that harm the environment [1–9]. They contaminate the natural environment through wastewater. In the last few years, the evaluation of water contamination by persistent micropollutants has directly affected the environment and is seriously harmful to human health. The latter is attracting increasing interest [10,11]. In addition, the problematics of treating these recalcitrant pollutants is a complex subject because the concept usually resides in the treatment of a high flow and weakly charged effluent, but constituted of a very complex pollution [12].

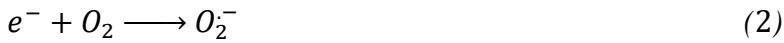
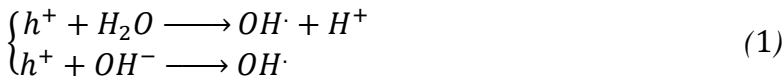
The development of the industry has generated an enormous production of wastewater, sometimes very difficult to treat by classical processes such as activated sludge or simple coagulation and flocculation [13–15]. However, these methods have shown their limits when faced with recalcitrant pollutants such as BTEX (benzene, toluene, ethylbenzene, and xylenes) and endocrine disruptors [16]. Among modern wastewater treatments, the photocatalytic degradation of various types of organic pollutants using solid semiconductors as photocatalysts has been widely studied (defined as heterogeneous photocatalysis). Which represents one of the typical advanced oxidation methods uses various semiconductor materials::  $\text{TiO}_2$ ,  $\text{ZnO}$ ,  $\text{CuO}$ ,  $\text{Bi}_2\text{O}_3$ , and  $\text{WO}_3$  [17–21].

Titanium dioxides ( $\text{TiO}_2$ ) are one of the commercial and common semiconductors that can be employed in photocatalysis for the photodegradation of organic molecules,  $\text{CO}_2$  conversion, and the hydrogen production [19,20,22]. Furthermore, non-toxic and inexpensive  $\text{TiO}_2$  exhibits high chemical and structural stabilities in its nature [23,24].  $\text{TiO}_2$  is a typical *n*-type semiconductor of transition metals and crystallises in different crystallographic forms, with the most abundant phases being anatase, rutile, and brookite [20]. Its photocatalytic activity often well acts under an ultraviolet (UV) light source, which limits its use for commercial and industrial applications. This is because the UV light occupies for approximately 7% of solar radiation [25]. The main limitation of  $\text{TiO}_2$  results from its wide band gap ( $E_g = 3.0\text{--}3.2$  eV) and the fast recombination of charge carriers [20,26–28]. Therefore, it is necessary to improve its absorption under visible ranges by changing its  $E_g$  values. Photocatalysis is the activation of semiconductors under visible, UV, or solar light sources. This energy causes the transition of an electron from his position in valence band to the conduction band. This process is known as the generation of electron–hole pairs (Eq. 1) [6,18,29] that initiate the photo-induced oxidation–reduction reactions by the generation of free radicals (Eqs. 2 and 3), that will either react with compounds present in the medium (i.e. dyes) (Eqs. 4,5), according to different mechanisms represented below [30–32].

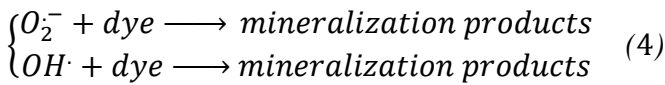
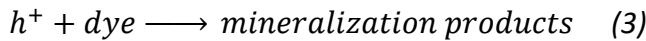
The first step is the excitation of the photocatalyst and formation of photo-induced charges:



The next step is the formation of hydroxide  $\text{OH}\cdot$ , and superoxide  $\text{O}_2^{\cdot-}$  radicals:



The degradation of the dye can be caused by the action of the holes ( $h^{+}$ ) directly or by the radicals generated by the ( $e^{-}$ ,  $h^{+}$ ) charges.



Many researchers tried to rise the photocatalytic activity of titanium oxide by using different methods such as incorporating metal(s) or non-metal(s) into catalysts or on the surface of catalysts. Among those approaches, the development of composites from  $\text{TiO}_2$  and semiconductors (using other transition metals:  $\text{CuO}$ ,  $\text{Fe}_2\text{O}_3$ , and  $\text{Bi}_2\text{O}_3$ ) is acknowledged as the best method for enhancing its photocatalytic activity. This combination can form heterojunction and simultaneously reduce the gap of  $\text{TiO}_2$ . It should improve the light absorption range and decrease recombination rate ( $e^{-}$  and  $h^{+}$ ) [22,27,33,34]. It is also well known that one of the inconveniences of using  $\text{TiO}_2$  is its low specific surface that makes the improvement of this surface even more interesting. This is done by attaching  $\text{TiO}_2$  or heterojunction based on  $\text{TiO}_2$  on an adsorbent (support) for example polymers, activated carbon, and clays (montmorillonite, kaolin, and zeolite) [28,35–37]. Zeolites (aluminosilicates) exhibit some proper properties such as good adsorbents due to their high specific area, structural stability, availability, and low cost [38,39]. Therefore, zeolite is used as appropriate carrier for loading catalysts on its external surface.

Several researchs have prepared the  $\text{TiO}_2$  heterojunction with other materials. Guerrero-Araque et al [40], prepared  $\text{Bi}_2\text{O}_3\text{--TiO}_2$  by the precipitation method co-catalysed by  $\text{CuO}$ ,  $\text{CoO}$ , or  $\text{NiO}$  using impregnation method. Sharma et al. [33], synthesized  $\text{Bi}_2\text{O}_3\text{--TiO}_2\text{--CuO}$  by the solution combustion. Zhao et al [41], used zeolite as a support for the  $\text{TiO}_2\text{--CuO}$  junction. Another example of the preparation of  $\text{TiO}_2\text{--CuO}$  supported on palygorskite clay is given in the paper of Lakbita et al. [42].

However, no study has been carried out on the support of the metal mixture ( $\text{TiO}_2\text{--Bi}_2\text{O}_3\text{--CuO}$ ) on clay, more precisely on a raw zeolite. In this work, the heterojunction  $\text{TiO}_2\text{--Bi}_2\text{O}_3\text{--CuO}$  was elaborated by the ceramic method and supported on a local natural clay under the ultrasonic waves.

The adsorption and photocatalysis performances of composite materials were studied under visible and solar light irradiation for evaluating the photodegradation of dye model (Safranin-O; SO). SO dye (**Table S1**) is a pink dye from the phenazine family [6,18]. Highly soluble in water and widely used in the tannery and textile industry for dyeing wool, cotton, fibers, paper, tannin, silk, and leather [43,44], it is also used in the biological sciences for staining in histology and cytology [45], for distinguishing bacterial species between different Gram (positive and negative) bacteria [46], and as a detector for LAMP amplicons [47]. Any existence of SO dye in wastewater would have harmful effects on water life. because it is known to be carcinogenic in the ecosystem [18,47,48]. In this investigation, an attempt is carried out to study the degradation of this dye in aqueous solution and textile wastewater charged with SO in the presence of  $\text{TiO}_2\text{-Bi}_2\text{O}_3\text{-CuO-Zeolite}$  catalyst in the dark and under visible/sunlight irradiation. Adsorption parameters such as contact times effect, adsorbent dose and initial concentration, and are optimized in darkness to achieve the highest elimination of SO dye from aqueous solutions. The adsorption process was estimated with kinetic and isotherm studies using a non-linear model. The nature of the irradiation as well as the CuO content and the effect of using zeolite as a matrix on the photodegradation yield were studied. The reaction rates were calculated using a first order nonlinear kinetic model. The performance of the supported catalyst on textile wastewater treatment has also been investigated.

## 2. Experiments

### 2.1. Materials

The commercial precursor materials used are bismuth oxide ( $\text{Bi}_2\text{O}_3$ ; Biochem), titanium oxide ( $\text{TiO}_2$ ; Biochem), copper oxide ( $\text{CuO}$ ; Biochem), silver nitrate ( $\text{AgNO}_3$ ; Sigma-Aldrich), Hydrochloric acid ( $\text{HCl}$ ; Sigma-Aldrich), and Safranin-O dye (Biochem). Those chemicals and solvents were of analytical grade and utilized without supplementary purification. Raw zeolite was obtained from Tinebdar-Bejaia, Algeria. The distilled water (DW) was used to prepare aqueous solutions, and ultra-pure water (UP) was used to rinse the zeolite. This is because the ultra-pure water contains almost no impurities compared to distilled water.

### 2.2. Preparation of $\text{TiO}_2\text{-Bi}_2\text{O}_3\text{-CuO}$ heterojunction

The material heterojunctions  $\text{TiO}_2\text{-}_x\text{Bi}_2\text{O}_3\text{-}_y\text{CuO}$  were prepared using a solid-state reaction method (**Figure S1**). In the composite  $[1-(x+y)] \text{TiO}_2\text{-}_x\text{Bi}_2\text{O}_3\text{-}_y\text{CuO}$ , the symbols  $x$  and  $y$  ( $= 5\text{-}30$  wt.%) are the weight fraction of  $\text{Bi}_2\text{O}_3$  and  $\text{CuO}$ , respectively.

#### 2.2.1. $\text{TiO}_2\text{-Bi}_2\text{O}_3\text{-CuO}$ synthesis

The TiO<sub>2</sub> and Bi<sub>2</sub>O<sub>3</sub> powders with different compositions (1-x)TiO<sub>2</sub>-xBi<sub>2</sub>O<sub>3</sub> (labelled as T-5B, T-10B, T-15B, T-20B, and T-25B) corresponded to x (wt.% = 5%, 10%, 15%, 20%, and 25%, respectively). After mixed and milled in a ceramic mortar for 2 h, they were calcined at 600 °C for 6 h.

An optical analysis was carried out by an Evolution 220 UV-vis spectrophotometer to determine the gap of each material, estimate the range of photoexcitation wavelengths, and evaluate the efficiency of photocatalytic degradation. For the next study, the fraction of compound Bi<sub>2</sub>O<sub>3</sub> was fixed at the 20 wt.% of TiO<sub>2</sub>

### ***2.2.2. Synthesis of TiO<sub>2</sub>-Bi<sub>2</sub>O<sub>3</sub>-CuO material***

The solid mixtures of three components [1-(0.2+y)]TiO<sub>2</sub>-0.2Bi<sub>2</sub>O<sub>3</sub>-yCuO were prepared through the similar procedure of the binary components. The samples containing Bi<sub>2</sub>O<sub>3</sub> (20%) and CuO (in different weight fractions: 5%–25%) were named as TB-5C, TB-10C, TB-15C, TB-20C, and TB-25C corresponding to y (CuO; wt.% = 5%, 10%, 15%, 20%, and 25%, respectively).

### ***2.2.3. Synthesis of TiO<sub>2</sub>-Bi<sub>2</sub>O<sub>3</sub>-CuO supported on raw zeolite***

The raw zeolite was ground (using a Planetary Mono Mill Fritsch Pulverisette 6) at 200 rpm for 2 h) and followed by rinsing with ultra-pure water, filtrating, and drying at 110 °C for 2h. The zeolite was then treated with HCl acid [49]. An appropriate quantity of zeolite was stirred in HCl solution (0.4 M) for 4 h. The sample was then rinsed until the total elimination of Cl<sup>-</sup> ions in the zeolite. The presence of Cl<sup>-</sup> ions was identified by a AgNO<sub>3</sub> method. The treated zeolite was dried at 105 °C. After that, the mixture of treated zeolite (0.35 g) and ultra-pure water (20 mL) was placed into an ultrasonic bath (Labsonic Falc, 50 KHz, ITALIE) for 30 min. Finally, the 0.15-g material (TB-20C) was dispersed in this mixture, treated during 30 min by an ultra sonic bath, stirred for 24 h, filtrated, and dried at 60 °C. The obtained supported catalyst was named as TBC-ZN.

## ***2.3. Equipment***

X-ray diffraction (XRD) measurement were carried out using an Empryan Panalytical diffractometer with copper target with CuKα radiation ( $\lambda = 0.154056$  nm) in the 2 $\theta$  range from 20° to 80°. The surface structure of the materials was examined using Thermoscientific Quattro S field emission scanning electron microscopy (SEM). The specific surface area of the samples was found by a BET surface analyzer Micromeritics, Gemini VII. Fourier-transform infrared (FT-IR) spectrum was measured with a Thermoscientific Nicolet IS50 FT-IR spectrometer. UV-vis absorption spectrum was measured by an Evolution 220 UV-visible spectrophotometer. Photoluminescence (PL)

spectrum was obtained by a Shimadzu 6000 spectrophotometer with an excitation wavelength of 360 nm.

#### 2.4. Synergy of adsorption and photocatalysis for Safranin-O dye removal

The adsorption capacity of various materials such as: natural zeolite and materials supported on natural zeolite, was determined using batch adsorption experiments. The support on zeolite optimized the adsorption capacity and improved the dye adsorption on the surface. In the other part, the adsorption capacity of the material is enhanced when it is supported on clay. These both phenomena are due to synergic effects and consequently increases the photocatalytic performance of the materials [3].

##### 2.4.1. Adsorption of Safranin-O dye

The adsorption experiments were performed in the dark environment using a beaker containing the dye solution (200 mL) and synthesized material. The 5 mL of the liquid was collected at regular intervals, and the dye concentrations were determined using the UV–visible spectrophotometry method ( $\lambda_{\max} = 520$  nm).

The kinetic study was carried out to determine the effect of contact time on dye adsorption process. Around 0.08 g of material (0.4 g/L) was mixed with  $V = 200$  mL of Safranin-O dye ( $C_o = 16$  mg/L). The experiments were realized in the dark at a room temperature. A suspension (5 mL) was taken at regular intervals for 5 h. The amount of Safranin-O dye adsorbed into material at any time  $t$  was calculated using the mass balance equation (Eq. 7). At equilibrium, the amount of Safranin-O dye adsorbed  $Q_e$  (mg/g) was determined as Eq. 8.

$$Q_t = \frac{C_o - C_t}{m} V \quad (7)$$

$$Q_e = \frac{C_o - C_e}{m} V \quad (8)$$

where  $C_o$  and  $C$ ,  $C_e$  (mg/L) are the initial concentrations at  $t=0$ , after a contact time  $t$  (min); and after equilibrium adsorption respectively.

##### 2.4.2. Photocatalytic degradation of Safranin-O dye

The photocatalytic efficiency of the synthesis catalyst was evaluate through the degradation of Safranin-O dye, the monitoring was done by measuring the dye absorbance  $a$  ( $\lambda_{\max} = 520$  nm). A decrease in absorbance at this wavelength represents the dye mineralization. The photocatalyst was introduced in a beaker containing 200 mL of dye solution at its given concentration.

A primary test indicated that the time required for adsorption–desorption equilibrium was around 60 min (data not shown). The system is maintained under magnetic stirring in darkness for 60 min. Then the sample was exposed to solar/visible (low power LED's) irradiation. The discoloration was measured by a spectrophotometer, by taking 5 mL of the solution every 1 h, after centrifugation (Hettich, Rotofix 32 A. Germany) for 10 min with at a speed of 3000 rpm), and the relative centrifugal force is 805 g – force. After that, the supernatant was analysed by a UV-visible spectrophotometer.

The percentage of mineralization has been determined by the following equation:

$$D(\%) = \frac{C_0 - C_t}{C_0} * 100 \quad (9)$$

where  $C_0 = C_{\text{ads}}$  is the concentration of dye after the adsorption and desorption equilibrium, and  $C_t$  is the concentration after a given time of degradation.

### 2.4.3. Application for removal of real wastewater

A real industrial effluent was collected from a local textile industry Algeria Manufacture of Various Textiles (Alfaditex, Remila, Bejaia). Approximate 0.08 g of sample was added to 200 mL of the effluent solution containing 16 mg/L and 20 mg/L of Safranin-O dye for the adsorption and photocatalytic experiments respectively. For the adsorption study, the suspension was stirred for 5 h in dark, at room temperature a volume has been collected every given time in order to determinate the equilibrium adsorption and desorption. The photocatalytic experience was launched under solar light. **Table S2** shows some basic properties of wastewater.

## 3. Properties of the prepared solids

### 3.1. Crystal characteristics of the materials

**Figure 1a** represents the XRD spectra of the unsupported materials. For the pure  $\text{TiO}_2$  sample, the anatase phase (JCPDS card No. 00-21-1272) was identified at  $2\theta$  of  $25.5^\circ$ ,  $37.2^\circ$ ,  $48.3^\circ$ ,  $54.1^\circ$ , and  $63.3^\circ$  corresponding to the planes (101), (103), (200), (105), and (204), respectively [22]. Some characteristic peaks of rutile phase (JCPDS: 00-21-1276) were detected at  $27.6^\circ$ ,  $36.3^\circ$ ,  $41.5^\circ$ , and  $76.6^\circ$  relating to the (110), (101), (111), and (202) planes, respectively. The  $\text{Bi}_2\text{O}_3$  solid indicated some peaks at  $27.75^\circ$ ,  $33.35^\circ$ ,  $46.51^\circ$ , and  $57.21^\circ$  (JCPDS: 01-072-0398) corresponding to the planes (120), (200), (223), and (024), respectively [27]. Some typical planes ( $-111$ ), (111), and ( $-311$ ) in the CuO sample (JCPDS: 10-074-1021) were reflected at  $2\theta$  of  $35.7^\circ$ ,  $38.9^\circ$ , and  $66.4^\circ$ , respectively. Notably all these compounds were detected in the binary (T-20B) and ternary (TB-25C) composites.

**Figure 1b** shows the spectrum of the natural zeolite (NZ) and the TB-25C material supported on zeolite (TBC-ZN). Several peaks observed at  $21.2^\circ$ ,  $23.4^\circ$ ,  $26.8^\circ$ , and  $30.2^\circ$  in ZN and TBC-ZN



were attributed to the (113), (501), (600), and (612) planes, respectively. They corresponded to the tetragonal phase of zeolite ZSM-5 (JCPDS: 00-044-0002). The other peaks indicated the presence of two other phases such as zeolite H-ZSM-5 (JCPDS: 01-080-0922) and zeolite Y (JCPDS: 01-077-1549). The XRD results confirmed that the  $\text{TiO}_2\text{-}0.2\text{Bi}_2\text{O}_3\text{-}0.25\text{CuO}$  (TB-25C) material has been successfully loaded on the zeolite.

### 3.2. Surface morphology of the materials

SEM images are presented in **Figure 2**. The SEM image of  $\text{TiO}_2$  (**Figure 2a**) indicated aggregates-formed nanoparticles with their sizes of 60–80 nm. T-20B showed a homogeneous grain distribution in its SEM image (**Figure 2b**). The particle size of T-20B increased significantly within the introduction of  $\text{Bi}_2\text{O}_3$  (100–160 nm). When CuO was added to T-20B, the particle size of resultant TB-25C reached 170 nm (**Figure 2c**). The growth in the sizes suggests the formation of *n-p* heterojunctions in the resultant materials.

**Figures 2d** and **2e** shows the surface morphology of the zeolite before and after acid treatment. Clearly, the surface of the clay was significantly modified by this treatment with an increase in the pores volume. The structure becomes more porous, which improved the adsorption capacity of this zeolite. When the material is supported on the zeolite (**Figure 2f**), the observed grains dispersed on the surface of the zeolite can be attributed to the TB-25C material, which causes the clogging of some pores and a decrease in the adsorption performance of the zeolite.

The EDS (**Figure S2**) analysis of all the samples showed a peak corresponding to carbon due to the nature of the carbonized film carrying the sample. The spectra of  $\text{TiO}_2$ , T-20B, and TB-25C confirmed the purity of the materials. The EDS spectrum of the zeolite consisted principally of Si, O, and Al elements, which results from the aluminosilicate structure. In addition to these chemical elements, other chemical compounds (Ca, Fe, Mg, and Ti) were observed in low amounts.

### 3.3. Textural property of the materials

Nitrogen adsorption isotherms of TB-25C, zeolite, and TBC-ZN at 77 K were studied, and the BET plots of those materials are shown in the **Figure S3**. The curve shows that the catalyst supported on the zeolite improves the amount of  $\text{N}_2$  adsorbed, the decrease in the amount of  $\text{N}_2$  adsorbed from TBC-ZN compared to zeolite confirms that the deposition of the catalyst particles on the zeolite causes blockage of the clay pores, as illustrated in the SEM images (**Figure 2**). The BET method was used to applied to estimate the surface areas ( $S_{\text{BET}}$ ) of materials. The  $S_{\text{BET}}$  values of TB-25C, zeolite and TBC-ZN was 2.81, 28.95, and 16.85  $\text{m}^2/\text{g}$ , respectively. A nearly similar result was reported by Liu et al [35]. Who synthesized  $\text{TiO}_2$  supported on zeolite ( $\text{TiO}_2\text{-zeolite}$ ) using sol-gel method. They concluded the  $S_{\text{BET}}$  value of zeolite decreased from 24.52 to 14.14  $\text{m}^2/\text{g}$  after loading

TiO<sub>2</sub> (TiO<sub>2</sub>/zeolite). This is because the TiO<sub>2</sub> particles blocked the zeolite's pores and incorporated inside the internal pores of the zeolite.

### 3.4. Surface functional group of the materials

**Figure 3a** and **3b** shows the IR spectrum of the natural zeolite, and the material supported on the zeolite. The band observed in the region 3500–3400 cm<sup>-1</sup>, was probably caused by the water's OH-groups vibrations [50]. A band appearing at around 476 cm<sup>-1</sup> (for TiO<sub>2</sub>, binary solution, ternary solution, and material supported on the zeolite) corresponds to the vibrations of the Ti–O and O–Ti–O bond [51]. A band at 839 and 1386 cm<sup>-1</sup> can be assigned to the elongation vibration of Bi–O–Bi and Bi–O bonds respectively [21]. The intensity of these bands was low in the binary solution compared to the pure Bi<sub>2</sub>O<sub>3</sub>, because of the low amount of Bi<sub>2</sub>O<sub>3</sub> present in T-20B. A band observed at 937 cm<sup>-1</sup> in the binary solution can be assigned to the Bi–O–Ti or Bi–O–Bi vibration [23]. A band at around 540 cm<sup>-1</sup> in the CuO spectrum probably involves the vibration of the Cu–O bond. The addition of CuO lead to decreasing the width of the band between 500 and 1000 cm<sup>-1</sup>. This is because CuO had a weak band in this region [52].

The FTIR spectrum of natural zeolite and the material supported on zeolite also showed a series of bands at 1030, 878, and 796 cm<sup>-1</sup> that are the typical characteristics of zeolite in the samples. A large band at 1030 cm<sup>-1</sup> can be ascribed to the vibration of the Si(Al)–O–Si(Al) chain. The bands at 878 and 796 cm<sup>-1</sup> were related to the vibration of the Si(Al)–O group [35,53]. A new low-intensity absorption band at 913 cm<sup>-1</sup> in TBC-ZN can result from the vibration of material–zeolite bond.

### 3.5. Optical properties of the materials

**Figure 4a** and **4b** shows the UV-visible absorption spectrum of the pure TiO<sub>2</sub>, binary solutions (T-xB) and ternary solutions (TB-yC), with  $x$  and  $y$  being 0–25 (wt.%). Bi<sub>2</sub>O<sub>3</sub> generated a slight improvement of the adsorption range when comparing to pure TiO<sub>2</sub> (**Figure 4a**). In **Figure 4b**, the spectra represented an adsorption queue under a visible region probably because of the  $d-d$  transition of copper in its oxide like CuO [40,41].

The Tauc equation was used to determine the gap energy of synthesized materials using the following formula [54]:

$$(\alpha hv)^{\frac{1}{2}} = K(hv - E_g) \quad (10)$$

where  $\alpha$  (2.303 A) is an optical absorption coefficient;  $K$  is a constant; and  $hv$  is a photon energy.

**Figure 4c** depicts the Tauc function  $(\alpha h\nu)^{1/2} = f(h\nu)$ . The extrapolation of the linear portion of the curve and intercept on energy axis gave the gap energies. The calculated values showed that the band gaps of the materials did not indicate a remarkable change within the additional presence of  $\text{Bi}_2\text{O}_3$  but their absorbances were improved. A decrease in  $E_g$  might result from the introduction of additional levels in the  $\text{TiO}_2$  optical band gap (**Table 1**).

### **3.6. Photoluminescence spectra of the materials**

The photoluminescence (PL) emission that is generally lower than the radiation used for excitation is a technique based on the detection of light emitted by the material. In essence, the intensity of the emitted photon depends highly on the rate of electron-hole recombination and the efficiency of the charge separation [20,55].

When the material has a low recombination, the signal of the PL tends to be low and the photocatalytic activity is important. Therefore, there is a correlation between the PL spectrum and photocatalytic performance. The PL spectra of the prepared materials and pure  $\text{TiO}_2$  are depicted in **Figure 5**. The spectrum of pure  $\text{TiO}_2$  showed some emission peaks at 387.1, 448.0, 465.7, 490.1 and 544.7 nm. The peak at 387.1 nm is assigned to the  $\text{TiO}_2$  gap [20,55]. The weak intensity peak detected at 448.0 nm was attributed to recombining between self-trapped electrons and holes [56,57]. The peaks between 465.7 nm and 544.7 nm might attributed to non-stoichiometric defects ( $\text{TiO}_{2-x}$  oxygen defect) and recombination of the latter with photoelectron [20,55–58]. The addition of  $\text{Bi}_2\text{O}_3$  and  $\text{CuO}$  into  $\text{TiO}_2$  reduces the intensity of the PL spectrum which improves the photocatalytic performance of the materials compared to pure  $\text{TiO}_2$ , and does not result in any further photoluminescence phenomena. A similar result was obtained by Sharma et al [33], who explained this phenomenon by  $\text{Bi}_2\text{O}_3$  and  $\text{CuO}$  behaving as an efficient medium for the transport of photoinduced charge species to the material surface. In the ternary solutions, except for composition TB-5C low intensity peaks were observed at 465.7 nm and 544.7 nm above this composition no peak was observed, indicating a strong charge separation which confirms the results of the photocatalytic experiments [33,59]. This result can be confirmed by the results of the photocatalytic experiments

## **4. Adsorption performance**

The effect of physico-chemical parameters on the adsorption capacity of materials, such as the adsorbent weight, the initial dye concentration, the contact time, and the nature of the solvent (distilled water/ textile wastewater) were studied.

### **4.1. Effect of adsorbent mass**

In order to estimate the effect of adsorbent amount, the different doses (0.2–0.5 g/L) of materials was studied at an initial SO dye concentration of 16 mg/L. **Figure S4** shows the effects of TBC-ZN weight on its adsorption capacity towards SO dye. The histograms showed that  $Q_e$  slightly decreased within an increase in the amount of doses used. A similar result is reported by Ayaden et al. [39] who used mordenite as adsorbent. The aggregation and accumulation of sites, as well as the number of unsaturated sites on the material's surface, rise as the adsorbent's weight increases [60,61], explaining a decrease in values  $Q_e$ . As a result, the weight of the material was established at 0.4 g/L for the remainder of this investigation.

#### **4.2. Effect of contact time and kinetic studies**

A kinetic adsorption experiment was conducted to determine the time necessary to obtain the adsorption equilibrium, in order to study the adsorption property of natural zeolite, pure TB-25C, and supported TB-25C on zeolite (noted TBC-ZN). The SO initial concentration was 16 mg/L and the materials amount was 0.08 g, either in distilled water or in the real industrial wastewater(200ml). The results are presented in **Figure 6**.

The curve shape shows that TBC is a poor adsorbent with almost zero adsorption capacity, while zeolite has good adsorption properties. However, when supporting the material on zeolite the adsorption capacity increases compared to the pure TBC, which may be due to the high specific surface area of the clay [24].

The first part of the kinetics is a short one, where the fixation of SO is very fast, it is realized in the first 50 min (for DW) and 100 min (for RW) of the adsorption. The presence of easily accessible sites, most probably on the solid external surfaces can explain this phenomena [62][63]. The second part is slower, and the adsorption rate is relatively low. This behaviour is well represented by a saturation level. This phenomenon can be justified by the dye diffusion surface to the less accessible adsorption sites [35]. The equilibrium time varied between 50 and 150 min for the model solution (**Figure 6a**) and the real wastewater (**Figure 6b**).

To better understand the nature of the kinetics in the adsorption process, two nonlinear models were applied in this study. Such as the pseudo-first order (PFO) model (Eq. 11) and pseudo-second-order (PSO) model (Eq. 12) [64].

$$Q_t = Q_e(1 - e^{-k_1 t}) \quad (11)$$

$$Q_t = \frac{k_2 Q_e^2 t}{1 + k_2 Q_e^2 t} \quad (12)$$

where  $k_1$  (1/min) represent the rate constant of the PFO model, and  $k_2$  [g/(mg×min)] is the rate constant of the PSO model.

As showed in **Table 2**, it is concluded that the model with the highest adjusted- $R^2$  and the lowest reduced- $\chi^2$  was the PSO model. This is in agreement with the critical reviews of Lima et al. [64] and of Tran et al. [65] who demonstrated that adsorption kinetics are usually described by this model. The values of the adsorbed quantity found in this model are very nearly to those of the experimental adsorbed quantities. Notably, different solvents used affected the adsorption capacity of TBC-ZN and the rate constant  $k_2$  of the kinetic adsorption (**Table 2**). The  $k_2$  value of the adsorption kinetics under the distilled water [0.0103 g/(mg×min)] was remarkably higher than that of (0.0062). However, the  $q_{e(\text{exp})}$  value of TBC-ZN under distilled water condition (22.76 mg/g) was similar to that of wastewater one (22.71 mg/g). The result suggest a great potential application of this material in reality treatments.

### 4.3. Adsorption isotherms and modelling

Adsorption isotherm  $Q_e = f(C_e)$  is the variation of the adsorbed quantity  $Q_e$  (mg/g) on a solid as a function of the concentration  $C_e$  (mg/L) of adsorbate at equilibrium under a given temperature. The experimental results of dye adsorption equilibrium (conducted in distilled water) by TBC-ZN were fitted by two isotherms: the Langmuir (**Eq. 13**) and Freundlich (**Eq. 14**) models. Those models are frequently applied in the literature [60,63,65,66].

$$Q_e = \frac{Q_{\max} K_L C_e}{1 + K_L C_e} \quad (13)$$

$$Q_e = K_F C_e^n \quad (14)$$

where  $Q_{\max}$  the Langmuir maximum amount of SO dye adsorbed by TBC-ZN (mg/g);  $K_L$  (L/mg) and  $K_F$  [(mg/g)/(mg/L)<sup>n</sup>] represents the sof the Langmuir and Freundlich model, respectively; and  $n$  is the empirical constants.

The adsorption isotherm and the result of modeling are provided in **Figure 7** and **Table 3**, respectively. The isotherm (**Figure 7**) indicated a concave down curve (increasing) and its shape was a L-type [67]. The result suggest that TBC-ZN exhibited a high adsorption affinity towards SO dye molecules when the dye concentrations increased. Although the Freundlich model presented the

higher adj- $R^2 = 0.972$  and lower red- $\chi^2$  than the Langmuir model. The maximum adsorption capacity of TBC-ZN for adsorbing SO dye (estimated based on the Langmuir model;  $Q_{\max} = 49.87$  mg/g) was remarkable lower than the corresponding value of activated carbon (221.8 mg/g) [68]. In essence, low adsorption capacities is often expected when it acts as catalysts and photo-catalysts.

## 5. Photocatalysis study

### 5.1. Preliminary photocatalysis test

The photocatalytic activity of the materials supported on zeolite were estimated through UV-visible and PL analyses combined with preliminary photocatalysis test under visible or solar lights. **Figure 8a** represents the photodegradation performance of the binary solution under visible light. The results showed that T-20B has the best photocatalytic activity. The materials (T-10B and T-15B) exhibited a relatively similar degradation efficiency which is in good agreement with the UV-visible result. The both compositions have a similar gap **Table 1**. Notably, the photodegradation efficiency of SO dye slightly decreased from 72.72% to 69.82% when the amount of  $\text{Bi}_2\text{O}_3$  increased from 20 wt.% (the T-20B sample) to 25 wt.% (T-25B). This might be because the  $p-p$  junctions were formed between  $\text{Bi}_2\text{O}_3$  and  $\text{Bi}_2\text{O}_3$  [33]. Police et al [25], explained such phenomenon resulting from raising the number of  $e^- - h^+$  recombination centers when the high amounts of  $\text{Bi}_2\text{O}_3$  was used.

Notably, an artificial light was used to provide electric energies consumed during the photocatalysis processes. The energy consumed during the experiments was measured using a Voltcraft (energy logger F4000). The result showed the energy consumption (approximately 5 kWh for degrading the dye solution: 16 mg/L and 200 mL) was not economically viable from commercial viewpoints. Therefore, the further experiments were carried out under a solar light.

**Figure 8b**, shows the impact of the amount of CuO added in the ternary solution on the dye discoloration efficiency of the resultant composites under sunlight. The result showed that TB-25C (containing 20%  $\text{Bi}_2\text{O}_3$  and 25% CuO) exhibited the highest photocatalytic activity (~43%) compared to the others (TB-10C, TB-15C, and TB-20C). This means that the photocatalytic activity increased with an increase in the amount of CuO added. Sharma et al [33], reported the optimal content of CuO in the composite was 10 wt.%. A higher content of CuO used (>10 wt.%) led to decreasing the performance of dye degradation. They explained that the formation of heterojunctions extended the life time of the charges by improving the movement of the ( $e^-$  and  $h^+$ ) charges when the CuO amount was below 10 wt.%. In contrast, when a higher amount of CuO was used (i.e., >than 10 wt.%), the catalyst activity of the composite decreased. This is because some CuO nanoparticles can act as a recombination center for electron-hole pairs, which reduces the photocatalytic activity [33].

The effect of the TB-25C supported on the zeolite (TBC-ZN) was examined under the solar irradiation at conditions: 0.4 g/L of the solid/liquid ratio and 20-mg/L dye solution (prepared in distilled water). **Figure 8b** shows TBC-ZN (80.5%) exhibited an excellent removal efficiency of SO dye compared to the materials unsupported on the zeolite (8.92%–19.03%). The percentage of dye removed by TBC-ZN (80.5%) was overwhelmingly higher than that by TB-25C (19.03%), which results from a higher specific surface area of TBC-ZN ( $S_{\text{BET}} = 16.85 \text{ m}^2/\text{g}$ ) than TB-25C ( $2.81 \text{ m}^2/\text{g}$ ). The TBC-ZN material with a higher  $S_{\text{BET}}$  value can generate more contact surface between the pollutant and the catalyst, which leads to a higher photo-catalytic performance [24]. The result is consistent with that of Rangkooy and co-workers who investigated the photodegradation of toluene using  $\text{TiO}_2$  and  $\text{TiO}_2$  supported on natural zeolite [69]. This confirms synergy effects between adsorption and photocatalysis efficiencies.

### **5.2. Dye removal efficiency by TBC-ZN under different water matrices**

The water matrices were prepared by dissolving SO dye solid in distilled water (denoted to SO-Distilled-Water) and real wastewater (SO-Wastewater). The effect of water matrices on the dye removal processes (by adsorption and photocatalysis) by TBC-ZN was explored at the initial SO dye concentration of ~20 mg/L (under the dark environment and solar irradiation, respectively).

**Figure 9** shows that after 4 h of solar irradiation, the initial concentration of SO decreased due to the simultaneous adsorption and mineralization of the dye. The adsorption efficiency of TBC-ZN was less affected by the different water matrices (~45%). However, the photodegradation was more efficiency in the case of SO–distilled water (89.07%) than in SO-Real wastewater (63.83%). The results may be due to the presence of other compounds decreasing the mineralization efficiency by a competition effect. Several authors have studied the degradation of the SO dye under visible or sunlight [18,70,71]. For example, PUCP1@rGO hybrid nanocomposite can remove 76% of the Safranin-O dye ( $C_0 = 5 \text{ }\mu\text{M}$  or 1.8 mg/L) in 90 min under visible light [70].

The kinetics and rate constant for photodegrading SO dye in distilled water and wastewater environments were studied using the Langmuir–Hinshelwood equation (Eq. 15) according to the nonlinear equation of the first order kinetic model [63]:

$$r = -\frac{dC_t}{dt} = \frac{kKC_t}{1 + KC_t} \quad (15)$$

where  $k$  [mg/(min×L)] and  $K$  (L/mg) represent the rate constant of photocatalytic and the adsorption constant respectively, and  $C_t$  is the concentration at time  $t$  (min).

When:

- $C_t$  is higher,  $KC_t$  increase, so the value of  $I + KC_t \approx KC_t$
- $C_t$  is lower,  $KC_t \ll I$ , so the denominator  $I + KC_t \approx I$

using these both mathematical theorems and under the low dye concentrations (~10 mg/L) employed in photocatalysis, the Langmuir–Hinshelwood equation becomes

$$-\frac{dC_t}{dt} = k_1 C_t \quad (16)$$

$$k_1 = k \times K \quad (17)$$

The integral of equation (19) gives:

$$\ln \frac{C_t}{C_o} = -k_1 t \quad (18)$$

where  $k_1$  (1/min) represents the rate constant of the first-order model.

When  $t = 0$  and  $C_t = C_o = B$ , the nonlinear equation can be simplified as follows:

$$C_t = C_o \times e^{-k_1 t} \quad (19)$$

According to **Figure 9**, the rate constant  $k_1$  (0.0062/min) and photodegradation efficiency (89.07%) of the system (TBC-ZN and SO-Distilled-Water) were higher than those (0.0050/min and 63.83%) of another (TBC-ZN and SO-Wastewater; **Table 4**). Therefore, the purity and nature of the water matrices greatly influenced both degradation rate and efficiency of SO dye. Some unknown organic compounds or solute ions in the wastewater can act as scavengers of radical (i.e., HO<sup>•</sup> generated during the photocatalysis) [73].

Furthermore, the mineralization of SO dye in wastewater, a total organic carbon (TOC) analysis was carried out using a TOC analyzer (Shimadzu TOC-VCSH, Japan), and the yield is calculated using the following formula:

$$R(\%) = \frac{TCO_i - TCO_f}{TCO_i} \times 100 \quad (20)$$

where  $TOC_i$  and  $TOC_f$  are the initial TOC and after irradiation time, respectively.

The data shows that the mineralization yield is approximately 68.2%, which is lower than the decolorization yield (80.23%) in real water. The above result can be explained by the formation of sub-products.

In the interest of understanding the charge transfer mechanism involved in the photodegradation of pollutants, according to the literature, the charge separation efficiency increases



considerably with the photocatalytic activity of the material [74]. In our case, the lifetime of the charge carriers is assured by the transfer of these carriers between the different energy levels of the oxides forming the ternary nanocomposite.

This phenomenon is reflected by the decrease in intensity of the PL spectra, on the other side it can be explained by a diagram that represents the conduction (CB) and valence (VB) band positions for each semiconductor. This is achieved by the use of the electronegativity concept [33,75]. the equation has been reported below:

$$E_{CB} = X - 4.5 - \frac{1}{2} E_g \quad (21)$$

$$E_{VB} = X - 4.5 + \frac{1}{2} E_g \quad (22)$$

where  $E_{CB}$  is the CB edge potential;  $E_{VB}$  is the VB edge potential;  $\chi$  is the electronegativity of the semiconductors;  $E_g$  is the band gap energy.

The values for CB and VB are shown in Table S3.

The presence of  $\text{TiO}_2$  between  $\text{Bi}_2\text{O}_3$  and  $\text{CuO}$  is supposed. From **Table S3**, before the contact, we find that the BC of  $\text{CuO}$  is more positive (+0.6 eV) than  $\text{Bi}_2\text{O}_3$  (0.053 eV) while VB of  $\text{Bi}_2\text{O}_3$  is more positive (2.01 eV) than  $\text{CuO}$  (2.01 eV). Furthermore, the BC of  $\text{Bi}_2\text{O}_3$  is more positive (+0.053 eV) than that of  $\text{TiO}_2$  while VB of  $\text{TiO}_2$  is more positive (2.828 eV) than that of  $\text{Bi}_2\text{O}_3$ . This case allows the transfer of the electron and the holes to the  $\text{CuO}$  bands, thus forming a type **I** system [76,77]. And it's well known that the fermi level for n-type semiconductors is close to the conduction band ( $\text{TiO}_2$ ), in contrast to the p-type semiconductor which is close to the valence band ( $\text{Bi}_2\text{O}_3$ ,  $\text{CuO}$ ). Based on the above results, the energy band diagram for  $\text{TiO}_2$ - $\text{Bi}_2\text{O}_3$ - $\text{CuO}$  is shown in **Figure 10a**.

Before the contact, the Fermi level of  $\text{TiO}_2$  is higher than that of  $\text{Bi}_2\text{O}_3$  and  $\text{CuO}$  has the lowest Fermi level [75,76,78]. Therefore, when two or more materials with different Fermi levels come into contact, electrons will be transferred from SC with a higher Fermi level ( $\text{TiO}_2$ ) to SC with the lower level  $\text{CuO}$  to see an equal level for all the composition [75]. Meanwhile, an internal electric field orienting  $\text{TiO}_2$  towards  $\text{Bi}_2\text{O}_3$  and  $\text{CuO}$  was built at the interface between them.

Therefore, a photocatalytic mechanism hypothesis of the  $\text{TiO}_2$ - $\text{Bi}_2\text{O}_3$ - $\text{CuO}$  heterojunction was illustrated below: under sunlight,  $\text{Bi}_2\text{O}_3$  and  $\text{CuO}$  can be easily excited by light and generated electrons and holes. From the **Figure.10b**, it can be seen that under the effect of an internal electric field, the electrons of the excited  $\text{Bi}_2\text{O}_3$  and  $\text{CuO}$  transferred to the conduction band of  $\text{TiO}_2$ , this

electron transition can improve the lifetime of the charge carriers, which also inhibited the recombination rate [76,77]. The shift of the band positions influences the type of heterojunction, Therefore, depending on the oxides band forming the ternary composite is type **II** system. The electrons present in the conduction band of TiO<sub>2</sub> can either be reacted with adsorbed O<sub>2</sub> to produce superoxide radicals [79], or recombine with the holes in the valence band of CuO for example, resulting in a **Z-Scheme** system [74,80]. The latter has a high charge separation performance and therefore a very high photocatalytic activity. The vacant sites in the VB of the oxides forming the heterosystem can also react with substances present in the reaction medium such as H<sub>2</sub>O and OH<sup>-</sup> forming highly reactive free radicals (Eq 2). Which can give rise to a series of reactions resulting in the degradation of dye molecules into a less harmful by-product and CO<sub>2</sub> [33].

## 6. Conclusions

In this study, n-p heterojunction catalysts (TiO<sub>2</sub>-Bi<sub>2</sub>O<sub>3</sub>-CuO) were synthesized via the ceramic method and supported on natural zeolite using wet impregnation under ultrasonic waves. We characterized the synthesized materials using various techniques and evaluated their photocatalytic properties for the mineralization of a cationic dye from distilled water and wastewater from a local textile dyeing plant. Our results indicate that the addition of Bi<sub>2</sub>O<sub>3</sub> and CuO to TiO<sub>2</sub> leads to the formation of pure crystalline structures with an ordered distribution of sphere-shaped grains. The introduction of Bi<sub>2</sub>O<sub>3</sub> shifts the absorption spectrum towards the visible region, while the addition of CuO creates an adsorption queue throughout the visible region. The best photocatalytic activity was achieved with TB-25C, which contained 20% Bi<sub>2</sub>O<sub>3</sub> and 25% CuO. The activity was attributed to the formation of heterojunctions, which led to strong charge separation. Furthermore, the support on clay increased the mineralization capacity, indicating the synergy between adsorption and photocatalysis. Despite the promising results, there are limitations to this study that should be addressed in future work. For instance, the photocatalytic activity of the synthesized catalysts can be further optimized by varying the synthesis conditions, such as the calcination temperature and time. Additionally, the stability and reusability of the catalysts should be evaluated to determine their potential for practical applications. In terms of applications, the synthesized catalysts have potential for use in wastewater treatment, particularly in the removal of cationic dyes from textile wastewater. Furthermore, the use of natural zeolite as a support material is environmentally friendly and cost-effective, making it an attractive alternative to synthetic supports. In conclusion, our study provides valuable insights into the elaboration and characterization of n-p heterosystems catalysts and their photocatalytic properties for the removal of cationic dyes. Future work should focus on optimizing

the synthesis conditions and evaluating the stability and reusability of the catalysts, as well as exploring their potential for practical applications in wastewater treatment.

## References

- [1] N. Bouchelkia, H. Tahraoui, A. Amrane, H. Belkacemi, J.-C. Bollinger, A. Bouzaza, A. Zoukel, J. Zhang, L. Mouni, Jujube stones based highly efficient activated carbon for methylene blue

- adsorption: Kinetics and isotherms modeling, thermodynamics and mechanism study, optimization via response surface methodology and machine learning approaches, *Process Saf. Environ. Prot.* 170 (2023) 513–535. <https://doi.org/10.1016/j.psep.2022.12.028>
- [2] S. Farch, M.M. Yahoum, S. Toumi, H. Tahraoui, S. Lefnaoui, M. Kebir, M. Zamouche, A. Amrane, J. Zhang, A. Hadadi, Application of Walnut Shell Biowaste as an Inexpensive Adsorbent for Methylene Blue Dye: Isotherms, Kinetics, Thermodynamics, and Modeling, *Separations*. 10 (2023) 60. <https://doi.org/10.3390/separations10010060>
- [3] Y. Yu, W. Xu, J. Fang, D. Chen, T. Pan, W. Feng, Y. Liang, Z. Fang, Soft-template assisted construction of superstructure TiO<sub>2</sub>/SiO<sub>2</sub>/g-C<sub>3</sub>N<sub>4</sub> hybrid as efficient visible-light photocatalysts to degrade berberine in seawater via an adsorption-photocatalysis synergy and mechanism insight, *Appl. Catal. B Environ.* 268 (2020) 118751. <https://doi.org/10.1016/j.apcatb.2020.118751>.
- [4] D.S. Firak, L. Farkas, M. Náfrádi, T. Alapi, Degradation of chlorinated and hydroxylated intermediates in UVA/CIO<sub>2</sub> systems: A chlorine-based advanced oxidation process investigation, *J. Environ. Chem. Eng.* 10 (2022) 107554. <https://doi.org/10.1016/j.jece.2022.107554>.
- [5] O. Baaloudj, A.K. Badawi, H. Kenfoud, Y. Benrighi, R. Hassan, N. Nasrallah, A.A. Assadi, Techno-economic studies for a pilot-scale Bi<sub>12</sub>TiO<sub>20</sub> based photocatalytic system for pharmaceutical wastewater treatment: From laboratory studies to commercial-scale applications, *J. Water Process Eng.* 48 (2022) 102847. <https://doi.org/10.1016/j.jwpe.2022.102847>.
- [6] M. El-Kemary, Y. Abdel-Moneam, M. Madkour, I. El-Mehasseb, Enhanced photocatalytic degradation of Safranin-O by heterogeneous nanoparticles for environmental applications, *J. Lumin.* 131 (2011) 570–576. <https://doi.org/10.1016/j.jlumin.2010.10.025>.
- [7] Y. Dong, H. Yuan, L. Bai, D. Ge, N. Zhu, A comprehensive study on simultaneous enhancement of sludge dewaterability and elimination of polycyclic aromatic hydrocarbons by Fe<sup>2+</sup> catalyzing O<sub>3</sub> process, *Sci. Total Environ.* 819 (2022) 152015. <https://doi.org/10.1016/j.scitotenv.2021.152015>.
- [8] T. Ahmad, M. Rafatullah, A. Ghazali, O. Sulaiman, R. Hashim, A. Ahmad, Removal of Pesticides from Water and Wastewater by Different Adsorbents: A Review, *J. Environ. Sci. Health Part C*. 28 (2010) 231–271. <https://doi.org/10.1080/10590501.2010.525782>.
- [9] L. Qian, L. Ding, W. Liu, S. Ren, H. Long, Simultaneous removal of NO and dioxins over V<sub>2</sub>O<sub>5</sub>-WO<sub>3</sub>/TiO<sub>2</sub> catalyst for iron ore sintering flue gas: The poisoning effect of Pb, *Fuel*. 324 (2022) 124483. <https://doi.org/10.1016/j.fuel.2022.124483>.
- [10] M.J. Moerland, K. van Gijn, X. Ji, C.J.N. Buisman, H.H.M. Rijnaarts, A.A.M. Langenhoff, M.H.A. van Eekert, Micropollutants removal during high rate thermophilic and hyper-thermophilic anaerobic digestion of concentrated black water, *J. Environ. Chem. Eng.* 10 (2022) 107340. <https://doi.org/10.1016/j.jece.2022.107340>.
- [11] P. Bhatt, G. Bhandari, M. Bilal, Occurrence, toxicity impacts and mitigation of emerging micropollutants in the aquatic environments: Recent tendencies and perspectives, *J. Environ. Chem. Eng.* 10 (2022) 107598. <https://doi.org/10.1016/j.jece.2022.107598>.
- [12] J. Cai, B. Niu, Q. Xie, N. Lu, S. Huang, G. Zhao, J. Zhao, Accurate Removal of Toxic Organic Pollutants from Complex Water Matrices, *Environ. Sci. Technol.* 56 (2022) 2917–2935. <https://doi.org/10.1021/acs.est.1c07824>.

- [13] A. Hadadi, A. Imessaoudene, J.-C. Bollinger, S. Cheikh, A.A. Assadi, A. Amrane, M. Kebir, L. Mouni, Parametrical Study for the Effective Removal of Mordant Black 11 from Synthetic Solutions: Moringa oleifera Seeds' Extracts Versus Alum, *Water*. 14 (2022) 4109. <https://doi.org/10.3390/w14244109>
- [14] B. Li, J. Zhao, W. Ge, W. Li, H. Yuan, Coagulation-flocculation performance and floc properties for microplastics removal by magnesium hydroxide and PAM, *J. Environ. Chem. Eng.* 10 (2022) 107263. <https://doi.org/10.1016/j.jece.2022.107263>.
- [15] W. Chu, Dye Removal from Textile Dye Wastewater Using Recycled Alum Sludge, *Water Res.* 35 (2001) 3147–3152. [https://doi.org/10.1016/S0043-1354\(01\)00015-X](https://doi.org/10.1016/S0043-1354(01)00015-X).
- [16] S. Salehi, K. Abdollahi, R. Panahi, N. Rahmanian, M. Shakeri, B. Mokhtarani, Applications of Biocatalysts for Sustainable Oxidation of Phenolic Pollutants: A Review, *Sustainability*. 13 (2021) 8620. <https://doi.org/10.3390/su13158620>.
- [17] S. Cheikh, A. Imessaoudene, J.-C. Bollinger, A. Hadadi, A. Manseri, A. Bouzaza, A. Assadi, A. Amrane, M. Zamouche, A. El Jery, Complete Elimination of the Ciprofloxacin Antibiotic from Water by the Combination of Adsorption–Photocatalysis Process Using Natural Hydroxyapatite and TiO<sub>2</sub>, *Catalysts*. 13 (2023) 336. <https://doi.org/10.3390/catal13020336>
- [18] K. Hayat, M.A. Gondal, M.M. Khaled, Z.H. Yamani, S. Ahmed, Laser induced photocatalytic degradation of hazardous dye (Safranin-O) using self synthesized nanocrystalline WO<sub>3</sub>, *J. Hazard. Mater.* 186 (2011) 1226–1233. <https://doi.org/10.1016/j.jhazmat.2010.11.133>.
- [19] A. Kane, A.A. Assadi, A. El Jery, A.K. Badawi, H. Kenfoud, O. Baaloudj, A.A. Assadi, Advanced Photocatalytic Treatment of Wastewater Using Immobilized Titanium Dioxide as a Photocatalyst in a Pilot-Scale Reactor: Process Intensification, *Materials*. 15 (2022) 4547. <https://doi.org/10.3390/ma15134547>.
- [20] P. Seeharaj, N. Vittayakorn, J. Morris, P. Kim-Lohsoontorn, CeO<sub>2</sub>/CuO/TiO<sub>2</sub> heterojunction photocatalysts for conversion of CO<sub>2</sub> to ethanol, *Nanotechnology*. 32 (2021) 375707. <https://doi.org/10.1088/1361-6528/ac08be>.
- [21] Y. Astuti, B.M. Listyani, L. Suyati, A. Darmawan, Bismuth Oxide Prepared by Sol-Gel Method: Variation of Physicochemical Characteristics and Photocatalytic Activity Due to Difference in Calcination Temperature, *Indones. J. Chem.* 21 (2020) 108. <https://doi.org/10.22146/ijc.53144>.
- [22] N. Lakshmana Reddy, S. Emin, M. Valant, M.V. Shankar, Nanostructured Bi<sub>2</sub>O<sub>3</sub>@TiO<sub>2</sub> photocatalyst for enhanced hydrogen production, *Int. J. Hydrog. Energy*. 42 (2017) 6627–6636. <https://doi.org/10.1016/j.ijhydene.2016.12.154>.
- [23] K. Lv, H. Zuo, J. Sun, K. Deng, S. Liu, X. Li, D. Wang, (Bi, C and N) codoped TiO<sub>2</sub> nanoparticles, *J. Hazard. Mater.* 161 (2009) 396–401. <https://doi.org/10.1016/j.jhazmat.2008.03.111>.
- [24] A. Mishra, A. Mehta, S. Basu, Clay supported TiO<sub>2</sub> nanoparticles for photocatalytic degradation of environmental pollutants: A review, *J. Environ. Chem. Eng.* 6 (2018) 6088–6107. <https://doi.org/10.1016/j.jece.2018.09.029>.
- [25] A.K.R. Police, S.V.P. Vattikuti, K.K. Mandari, M. Chennaiahgari, P.S. M.V., D.K. Valluri, C. Byon, Bismuth oxide cocatalyst and copper oxide sensitizer in Cu<sub>2</sub>O/TiO<sub>2</sub>/Bi<sub>2</sub>O<sub>3</sub> ternary photocatalyst for efficient hydrogen production under solar light irradiation, *Ceram. Int.* 44 (2018) 11783–11791. <https://doi.org/10.1016/j.ceramint.2018.03.262>.

- [26] R. Huber, J.-E. Moser, M. Grätzel, J. Wachtveitl, Real-Time Observation of Photoinduced Adiabatic Electron Transfer in Strongly Coupled Dye/Semiconductor Colloidal Systems with a 6 fs Time Constant, *J. Phys. Chem. B.* 106 (2002) 6494–6499. <https://doi.org/10.1021/jp0155819>.
- [27] A.K. Chakraborty, M.E. Hossain, M.M. Rhaman, K. Sobahan, Fabrication of Bi<sub>2</sub>O<sub>3</sub>/TiO<sub>2</sub> nanocomposites and their applications to the degradation of pollutants in air and water under visible-light, *J. Environ. Sci.* 26 (2014) 458–465. [https://doi.org/10.1016/S1001-0742\(13\)60428-3](https://doi.org/10.1016/S1001-0742(13)60428-3).
- [28] M. Malika, S.S. Sonawane, Statistical modelling for the Ultrasonic photodegradation of Rhodamine B dye using aqueous based Bi-metal doped TiO<sub>2</sub> supported montmorillonite hybrid nanofluid via RSM, *Sustain. Energy Technol. Assess.* 44 (2021) 100980. <https://doi.org/10.1016/j.seta.2020.100980>.
- [29] M.A.U. Olea, J. de J.P. Bueno, A.X.M. Pérez, Nanometric and surface properties of semiconductors correlated to photocatalysis and photoelectrocatalysis applied to organic pollutants – A review, *J. Environ. Chem. Eng.* 9 (2021) 106480. <https://doi.org/10.1016/j.jece.2021.106480>.
- [30] S. Chaudhuri, C.-M. Wu, K.G. Motora, Highly efficient solar-light-driven self-floatable WO<sub>2</sub>.72@ Fe<sub>3</sub>O<sub>4</sub> immobilized cellulose nanofiber aerogel/polypropylene Janus membrane for interfacial photocatalysis, *J. Photochem. Photobiol. Chem.* (2022) 114525. <https://doi.org/10.1016/j.jphotochem.2022.114525>
- [31] M. Zulfiqar, M.F.R. Samsudin, S. Sufian, Modelling and optimization of photocatalytic degradation of phenol via TiO<sub>2</sub> nanoparticles: An insight into response surface methodology and artificial neural network, *J. Photochem. Photobiol. Chem.* 384 (2019) 112039. <https://doi.org/10.1016/j.jphotochem.2019.112039>
- [32] F.C. Monteiro, I.D.L. Guimaraes, P. de Almeida Rodrigues, J.V. da A. de Pinho, C.A. Conte-Junior, Degradation of PAHs using TiO<sub>2</sub> as a semiconductor in the heterogeneous photocatalysis process: a systematic review, *J. Photochem. Photobiol. Chem.* (2022) 114497. <https://doi.org/10.1016/j.jphotochem.2022.114497>
- [33] S. Sharma, N. Kumar, B. Mari, N.S. Chauhan, A. Mittal, S. Maken, K. Kumari, Solution combustion synthesized TiO<sub>2</sub>/Bi<sub>2</sub>O<sub>3</sub>/CuO nano-composites and their photocatalytic activity using visible LEDs assisted photoreactor, *Inorg. Chem. Commun.* 125 (2021) 108418. <https://doi.org/10.1016/j.inoche.2020.108418>.
- [34] O.F.S. Khasawneh, P. Palaniandy, M. Ahmadipour, H. Mohammadi, M.R. Bin Hamdan, Removal of acetaminophen using Fe<sub>2</sub>O<sub>3</sub>-TiO<sub>2</sub> nanocomposites by photocatalysis under simulated solar irradiation: Optimization study, *J. Environ. Chem. Eng.* 9 (2021) 104921. <https://doi.org/10.1016/j.jece.2020.104921>.
- [35] X. Liu, Y. Liu, S. Lu, W. Guo, B. Xi, Performance and mechanism into TiO<sub>2</sub>/Zeolite composites for sulfadiazine adsorption and photodegradation, *Chem. Eng. J.* 350 (2018) 131–147. <https://doi.org/10.1016/j.cej.2018.05.141>.
- [36] J. Lin, Y. Tao, J. Liu, C. Zheng, X. Song, P. Dai, Q. Wang, W. Li, W. Chen, TiO<sub>2</sub>@carbon microsphere core-shell micromotors for photocatalytic water remediation, *Opt. Mater.* 124 (2022) 111989. <https://doi.org/10.1016/j.optmat.2022.111989>.
- [37] M.S. Rajan, M. Yoon, J. Thomas, Kaolin-graphene carboxyl incorporated TiO<sub>2</sub> as efficient visible light active photocatalyst for the degradation of cefuroxime sodium, *Photochem. Photobiol. Sci.* 21 (2022) 509–528. <https://doi.org/10.1007/s43630-022-00179-2>.

- [38] A. Imessaoudene, S. Cheikh, A. Hadadi, N. Hamri, J.-C. Bollinger, A. Amrane, H. Tahraoui, A. Manseri, L. Mouni, Adsorption Performance of Zeolite for the Removal of Congo Red Dye: Factorial Design Experiments, Kinetic, and Equilibrium Studies, *Separations*. 10 (2023) 57. <https://doi.org/10.3390/separations10010057>
- [39] B. Ayaden, N. Benabdeslam, N. Bouzidi, L. Mahtout, M. Bounouala, D. Merabet, Natural mordenite-rich tuff as an alternative for removing textile dyes (Asucryl red): adsorption properties, kinetic and equilibrium studies, *Clay Miner.* 54 (2019) 349–355. <https://doi.org/10.1180/clm.2019.47>.
- [40] D. Guerrero-Araque, D. Ramírez-Ortega, H.A. Calderon, J.M. Saniger, R. Gómez, Effect of Co-catalyst (CuO, CoO or NiO) on Bi<sub>2</sub>O<sub>3</sub>-TiO<sub>2</sub> structures and its impact on the photocatalytic reduction of 4-nitrophenol, *Top. Catal.* 64 (2021) 112–120. <https://doi.org/10.1007/s11244-020-01335-7>
- [41] L. Zhao, T. Cui, Y. Li, B. Wang, J. Han, L. Han, Z. Liu, Efficient visible light photocatalytic activity of p–n junction CuO/TiO<sub>2</sub> loaded on natural zeolite, *RSC Adv.* 5 (2015) 64495–64502. <https://doi.org/10.1039/C5RA07597A>
- [42] O. Lakbita, B. Rhouta, F. Maury, F. Senocq, M. Amjoud, A. Jada, Laser induced photocatalytic, *J. Colloid Sci. Biotechnol.* 5 (2016) 199–205. <https://doi.org/10.1166/jcsb.2016.1150>
- [43] V. Chandane, V. Singh, Adsorption of safranin dye from aqueous solutions using a low-cost agro-waste material soybean hull, *Desalination Water Treat.* 57 (2016) 4122–4134. <https://doi.org/10.1080/19443994.2014.991758>
- [44] F.H. Abdullah, M. Rauf, S.S. Ashraf, Photolytic oxidation of Safranin-O with H<sub>2</sub>O<sub>2</sub>, *Dyes Pigments*. 72 (2007) 349–352. <https://doi.org/10.1016/j.dyepig.2005.09.015>
- [45] M.G. Domingo, G.A. Nalli, D.R. Tasat, D.G. Olmedo, Exfoliated oral mucosa cells as bioindicators of short-and long-term systemic titanium contamination, *J. Trace Elem. Med. Biol.* 76 (2023) 127114. <https://doi.org/10.1016/j.jtemb.2022.127114>
- [46] P. Savadori, S. Dalfino, M. Piazzoni, M. Parrini, M. Del Fabbro, G.M. Tartaglia, L. Giardino, A simplified method for detecting Gram-positive and Gram-negative bacteria in dental histological samples: A preliminary and comparative study, *Acta Histochem.* 125 (2023) 151992. <https://doi.org/10.1016/j.acthis.2022.151992>
- [47] V.P. Dinh, N.Y. Lee, Fabrication of a fully integrated paper microdevice for point-of-care testing of infectious disease using Safranin O dye coupled with loop-mediated isothermal amplification, *Biosens. Bioelectron.* 204 (2022) 114080. <https://doi.org/10.1016/j.bios.2022.114080>
- [48] P.M. Pakdel, S.J. Peighamardoust, N. Arsalani, H. Aghdasinia, Safranin-O cationic dye removal from wastewater using carboxymethyl cellulose-grafted-poly (acrylic acid-co-itaconic acid) nanocomposite hydrogel, *Environ. Res.* 212 (2022) 113201. <https://doi.org/10.1016/j.envres.2022.113201>
- [49] A.P. Aziztyana, S. Wardhani, Y.P. Prananto, D. Purwonugroho, Darjito, Optimisation of Methyl Orange Photodegradation Using TiO<sub>2</sub>-Zeolite Photocatalyst and H<sub>2</sub>O<sub>2</sub> in Acid Condition, *IOP Conf. Ser. Mater. Sci. Eng.* 546 (2019) 042047. <https://doi.org/10.1088/1757-899X/546/4/042047>.

- [50] K. Cho, M.R. Hoffmann,  $\text{Bi}_x\text{Ti}_{1-x}\text{O}_z$  Functionalized Heterojunction Anode with an Enhanced Reactive Chlorine Generation Efficiency in Dilute Aqueous Solutions, *Chem. Mater.* 27 (2015) 2224–2233. <https://doi.org/10.1021/acs.chemmater.5b00376>.
- [51] S. Yin, Y. Chen, M. Li, Q. Hu, Y. Ding, Y. Shao, J. Di, J. Xia, H. Li, Construction of  $\text{NH}_2\text{-MIL-125(Ti)/Bi}_2\text{WO}_6$  composites with accelerated charge separation for degradation of organic contaminants under visible light irradiation, *Green Energy Environ.* 5 (2020) 203–213. <https://doi.org/10.1016/j.gee.2020.03.008>.
- [52] S. Zuo, D. Li, F. Yang, H. Xu, M. Huang, Z. Guan, D. Xia, Copper oxide/graphitic carbon nitride composite for bisphenol a degradation by boosted peroxymonosulfate activation: Mechanism of Cu-O covalency governs, *J. Colloid Interface Sci.* 603 (2021) 85–93. <https://doi.org/10.1016/j.jcis.2021.06.099>.
- [53] B. Ma, B. Lothenbach, Synthesis, characterization, and thermodynamic study of selected K-based zeolites, *Cem. Concr. Res.* 148 (2021) 106537. <https://doi.org/10.1016/j.cemconres.2021.106537>.
- [54] P. Makuła, M. Pacia, W. Macyk, How To Correctly Determine the Band Gap Energy of Modified Semiconductor Photocatalysts Based on UV–Vis Spectra, *J. Phys. Chem. Lett.* 9 (2018) 6814–6817. <https://doi.org/10.1021/acs.jpcclett.8b02892>.
- [55] N.N.T. Ton, A.T.N. Dao, K. Kato, T. Ikenaga, D.X. Trinh, T. Taniike, One-pot synthesis of  $\text{TiO}_2/\text{graphene}$  nanocomposites for excellent visible light photocatalysis based on chemical exfoliation method, *Carbon.* 133 (2018) 109–117. <https://doi.org/10.1016/j.carbon.2018.03.025>.
- [56] W. Alrashedi, Enhancement of the photocatalytic response of Cu-doped  $\text{TiO}_2$  nanotubes induced by the addition of strontium, *J. Photochem.* (2022). <https://doi.org/10.1016/j.jphotochem.2022.113858>
- [57] Y. Lei, L.D. Zhang, G.W. Meng, G.H. Li, X.Y. Zhang, C.H. Liang, W. Chen, S.X. Wang, Preparation and photoluminescence of highly ordered  $\text{TiO}_2$  nanowire arrays, *Appl. Phys. Lett.* 78 (2001) 1125–1127. <https://doi.org/10.1063/1.1350959>.
- [58] S. Mathew, A. kumar Prasad, T. Benoy, P.P. Rakesh, M. Hari, T.M. Libish, P. Radhakrishnan, V.P.N. Nampoori, C.P.G. Vallabhan, UV-Visible Photoluminescence of  $\text{TiO}_2$  Nanoparticles Prepared by Hydrothermal Method, *J. Fluoresc.* 22 (2012) 1563–1569. <https://doi.org/10.1007/s10895-012-1096-3>.
- [59] M.A. Gondal, M.A. Dastageer, S.G. Rashid, S.M. Zubair, M.A. Ali, D.H. Anjum, J.H. Lienhard, G.H. Mckinley, K. Varanasi, Plasmon Resonance Enhanced Photocatalysis Under Visible Light with  $\text{Au/Cu-TiO}_2$  Nanoparticles: Removal Cr (VI) from Water as a Case of Study, *Sci. Adv. Mater.* 5 (2013) 2007–2014. <https://doi.org/10.1166/sam.2013.1669>.
- [60] A. Imessaoudene, S. Cheikh, J.-C. Bollinger, L. Belkhiri, A. Tiri, A. Bouzaza, A. El Jery, A. Assadi, A. Amrane, L. Mouni, Zeolite Waste Characterization and Use as Low-Cost, Ecofriendly, and Sustainable Material for Malachite Green and Methylene Blue Dyes Removal: Box–Behnken Design, Kinetics, and Thermodynamics, *Appl. Sci.* 12 (2022) 7587. <https://doi.org/10.3390/app12157587>.
- [61] W.D. Wang, Y.X. Cui, L.K. Zhang, Y.M. Li, P. Sun, J.H. Han, Synthesis of a novel  $\text{ZnFe}_2\text{O}_4/\text{porous biochar}$  magnetic composite for  $\text{Th(IV)}$  adsorption in aqueous solutions, *Int. J. Environ. Sci. Technol.* 18 (2021) 2733–2746. <https://doi.org/10.1007/s13762-020-03023-1>.



- [62] S. Agarwal, A. Rani, Adsorption of resorcinol from aqueous solution onto CTAB/NaOH/flyash composites: Equilibrium, kinetics and thermodynamics, *J. Environ. Chem. Eng.* 5 (2017) 526–538. <https://doi.org/10.1016/j.jece.2016.11.035>.
- [63] A. Chedri Mammar, L. Mouni, J.-C. Bollinger, L. Belkhiri, A. Bouzaza, A.A. Assadi, H. Belkacemi, Modeling and optimization of process parameters in elucidating the adsorption mechanism of Gallic acid on activated carbon prepared from date stones, *Sep. Sci. Technol.* 55 (2020) 3113–3125. <https://doi.org/10.1080/01496395.2019.1676785>.
- [64] E.C. Lima, F. Sher, A. Guleria, M.R. Saeb, I. Anastopoulos, H.N. Tran, A. Hosseini-Bandegharai, Is one performing the treatment data of adsorption kinetics correctly?, *J. Environ. Chem. Eng.* 9 (2021) 104813.
- [65] H.N. Tran, S.-J. You, A. Hosseini-Bandegharai, H.-P. Chao, Mistakes and inconsistencies regarding adsorption of contaminants from aqueous solutions: A critical review, *Water Res.* 120 (2017) 88–116. <https://doi.org/10.1016/j.watres.2017.04.014>.
- [66] L. Mouni, L. Belkhiri, J.-C. Bollinger, A. Bouzaza, A. Assadi, A. Tirri, F. Dahmoune, K. Madani, H. Remini, Removal of Methylene Blue from aqueous solutions by adsorption on Kaolin: Kinetic and equilibrium studies, *Appl. Clay Sci.* 153 (2018) 38–45. <https://doi.org/10.1016/j.clay.2017.11.034>.
- [67] H.N. Tran, J.-C. Bollinger, S. Salvestrini, K.H. Chu, R.-S. Juang, Critical Review and Discussion of the Nonlinear Form of Radke–Prausnitz Model in Adsorption Solid–Liquid Phases, *J. Environ. Eng.* 149 (2023) 03122006.
- [68] Y.S. Reddy, N.K. Rotte, S. Hussain, V.V. Srikanth, M.R. Chandra, Sustainable mesoporous graphitic activated carbon as biosorbent for efficient adsorption of acidic and basic dyes from wastewater: Equilibrium, kinetics and thermodynamic studies, *J. Hazard. Mater. Adv.* 9 (2023) 100214. <https://doi.org/10.1016/j.hazadv.2022.100214>
- [69] H.A. Rangkooy, S. Mokaramian, B. Zargar, Photocatalytic Removal of Toluene Vapour Pollutant from the Air Using Titanium Dioxide Nanoparticles Supported on the Natural Zeolite, Iran. *J. Public Health.* 52 (2023) 184. [DOI:10.18502/ijph.v52i1.11681](https://doi.org/10.18502/ijph.v52i1.11681)
- [70] K. Arya, A. Kumar, A. Sharma, S. Singh, S.K. Sharma, S.K. Mehta, R. Kataria, A Hybrid Nanocomposite of Coordination Polymer and rGO for Photocatalytic Degradation of Safranin-O Dye Under Visible Light Irradiation, *Top. Catal.* (2022) 1–14. <https://doi.org/10.1016/j.matpr.2020.10.967>
- [71] EL-KEMARY, Maged, ABDEL-MONEAM, Yasser, MADKOUR, Metwally, *et al.* Enhanced photocatalytic degradation of Safranin-O by heterogeneous nanoparticles for environmental applications. *Journal of Luminescence*, 2011, vol. 131, no 4, p. 570-576. <https://doi.org/10.1016/j.jlumin.2010.10.025>
- [72] A.R. Amani-Ghadim, M.S.S. Dorraji, Modeling of photocatalytic process on synthesized ZnO nanoparticles: Kinetic model development and artificial neural networks, *Appl. Catal. B Environ.* 163 (2015) 539–546. <https://doi.org/10.1016/j.apcatb.2014.08.020>.
- [73] J.T. Schneider, D.S. Firak, R.R. Ribeiro, P. Peralta-Zamora, Use of scavenger agents in heterogeneous photocatalysis: truths, half-truths, and misinterpretations, *Phys. Chem. Chem. Phys.* 22 (2020) 15723–15733. <https://doi.org/10.1039/D0CP02411B>

- [74] J. Fernández-Catalá, R. Greco, M. Navlani-García, W. Cao, Á. Berenguer-Murcia, D. Cazorla-Amorós, g-C<sub>3</sub>N<sub>4</sub>-Based Direct Z-Scheme Photocatalysts for Environmental Applications, *Catalysts*. 12 (2022) 1137. <https://doi.org/10.3390/catal12101137>
- [75] S. Annathurai, S. Chidambaram, B. Baskaran, G. Prasanna Venkatesan, Green synthesis and electrical properties of p-CuO/n-ZnO heterojunction diodes, *J. Inorg. Organomet. Polym. Mater.* 29 (2019) 535–540. <https://doi.org/10.1007/s10904-018-1026-1>
- [76] N.T. Padmanabhan, N. Thomas, J. Louis, D.T. Mathew, P. Ganguly, H. John, S.C. Pillai, Graphene coupled TiO<sub>2</sub> photocatalysts for environmental applications: A review, *Chemosphere*. 271 (2021) 129506. <https://doi.org/10.1016/j.chemosphere.2020.129506>
- [77] A. Kubiak, Z. Bielan, M. Kubacka, E. Gabała, A. Zgoła-Grześkowiak, M. Janczarek, M. Zalas, A. Zielińska-Jurek, K. Siwińska-Ciesielczyk, T. Jesionowski, Microwave-assisted synthesis of a TiO<sub>2</sub>-CuO heterojunction with enhanced photocatalytic activity against tetracycline, *Appl. Surf. Sci.* 520 (2020) 146344. <https://doi.org/10.1016/j.apsusc.2020.146344>
- [78] S.S. Surah, M. Vishwakarma, R. Kumar, R. Nain, S. Sirohi, G. Kumar, Tuning the electronic band alignment properties of TiO<sub>2</sub> nanotubes by boron doping, *Results Phys.* 12 (2019) 1725–1731. <https://doi.org/10.1016/j.rinp.2019.01.081>
- [79] A. Hezam, K. Namratha, Q. Drmosh, Z. Yamani, K. Byrappa, Synthesis of heterostructured Bi<sub>2</sub>O<sub>3</sub>-CeO<sub>2</sub>-ZnO photocatalyst with enhanced sunlight photocatalytic activity, *Ceram. Int.* 43 (2017) 5292–5301. <https://doi.org/10.1016/j.ceramint.2017.01.059>
- [80] M.E. Aguirre, R. Zhou, A.J. Eugene, M.I. Guzman, M.A. Grela, Cu<sub>2</sub>O/TiO<sub>2</sub> heterostructures for CO<sub>2</sub> reduction through a direct Z-scheme: Protecting Cu<sub>2</sub>O from photocorrosion, *Appl. Catal. B Environ.* 217 (2017) 485–493. <https://doi.org/10.1016/j.apcatb.2017.05.058>

## List of Figures

**Figure 1.** XRD patterns of (a) unsupported materials, (b) zeolite and supported material.

**Figure 2.** SEM-EDX images of TBC and zeolite before and after acid treatment (a-f) SEM image (g) EDX spectra [and](#) (h) N<sub>2</sub> adsorption isotherms of the samples.

**Figure 3** FT-IR spectra of TBxCy and TBC-ZN

**Figure 4.** UV–visible spectra and Tauc equation

**Figure 5.** Photoluminescence spectra of different composite.

**Figure 6.** Adsorption kinetics of SO dye prepared in (a) distilled water (b) wastewater

**Figure 7.** Langmuir and Freundlich adsorption isotherms models for SO adsorption on TBC-ZN

**Figure 8.** a) Photocatalytic activity of binary solution under visible light, b) Photocatalytic activity of ternary solution and TB-25C supported on the raw zeolite under sunlight with  $m/V = 0.4$  g/L and  $C_0$  of dye = 20 mg/L

**Figure 9.** a) Effective removal of SO dye (prepared in distilled water and wastewater) by TBC-ZN by adsorption and photocatalysis processes and, b) UV–VIS absorption spectrum of SO dye in wastewater before and after photocatalysis

**Figure 10.** a) Energy band diagram of the TiO<sub>2</sub>, Bi<sub>2</sub>O<sub>3</sub> and CuO before the contact; b) Energy band diagram of the TBC heterojunction.

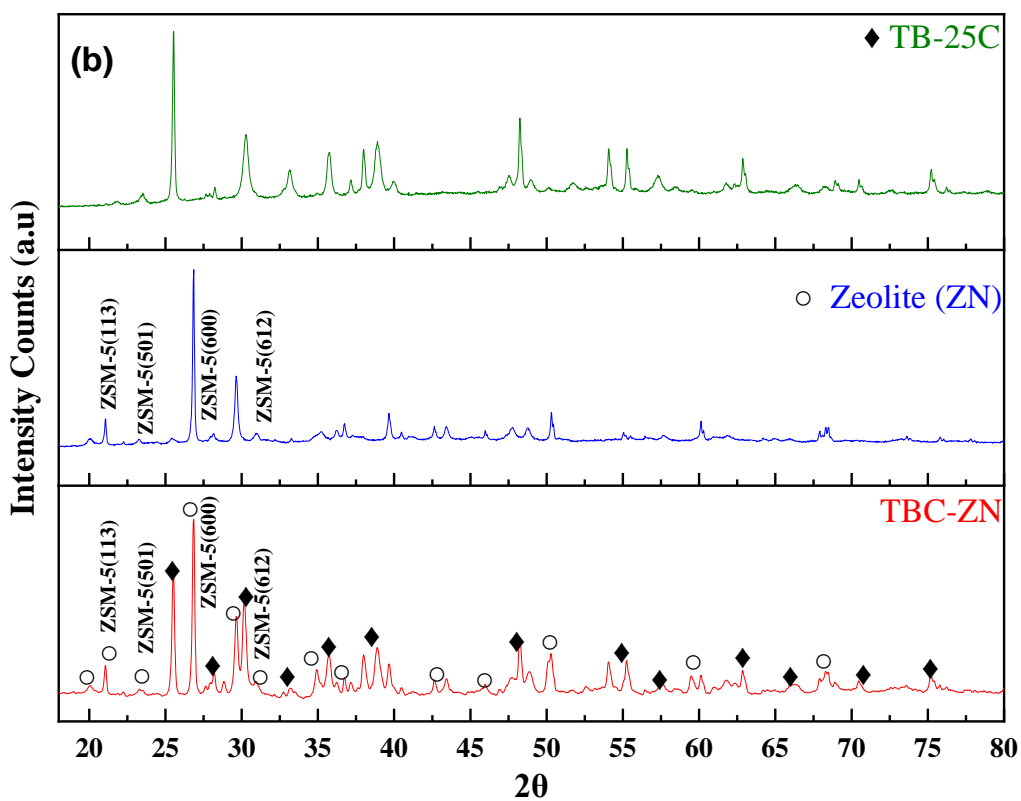
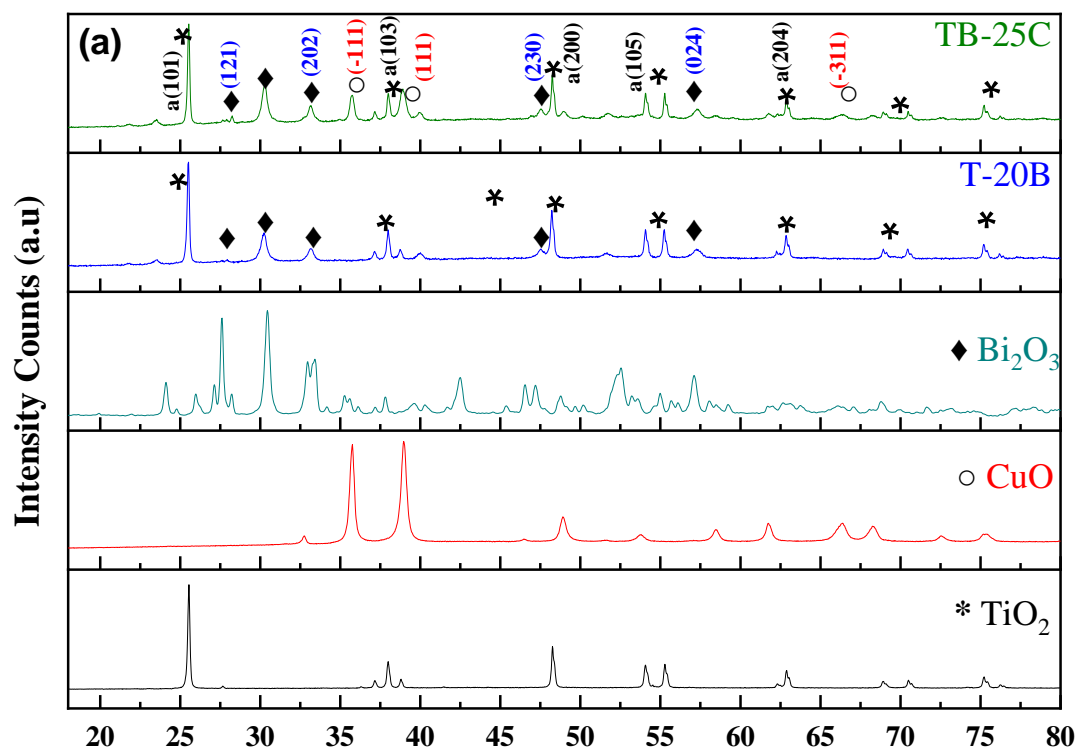


Figure 1. XRD patterns of (a) unsupported materials, and (b) zeolite and supported material.

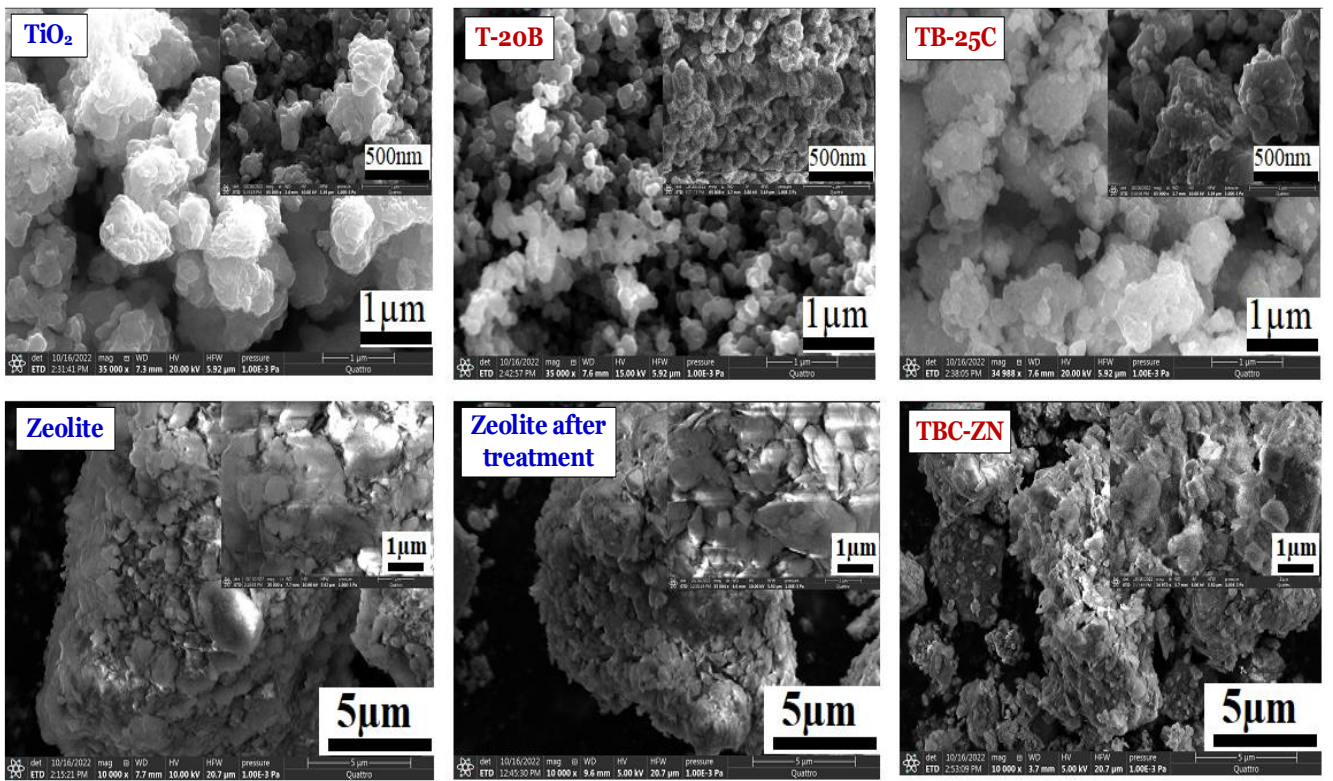


Figure 2. SEM images of TBC and zeolite before and after acid treatment.

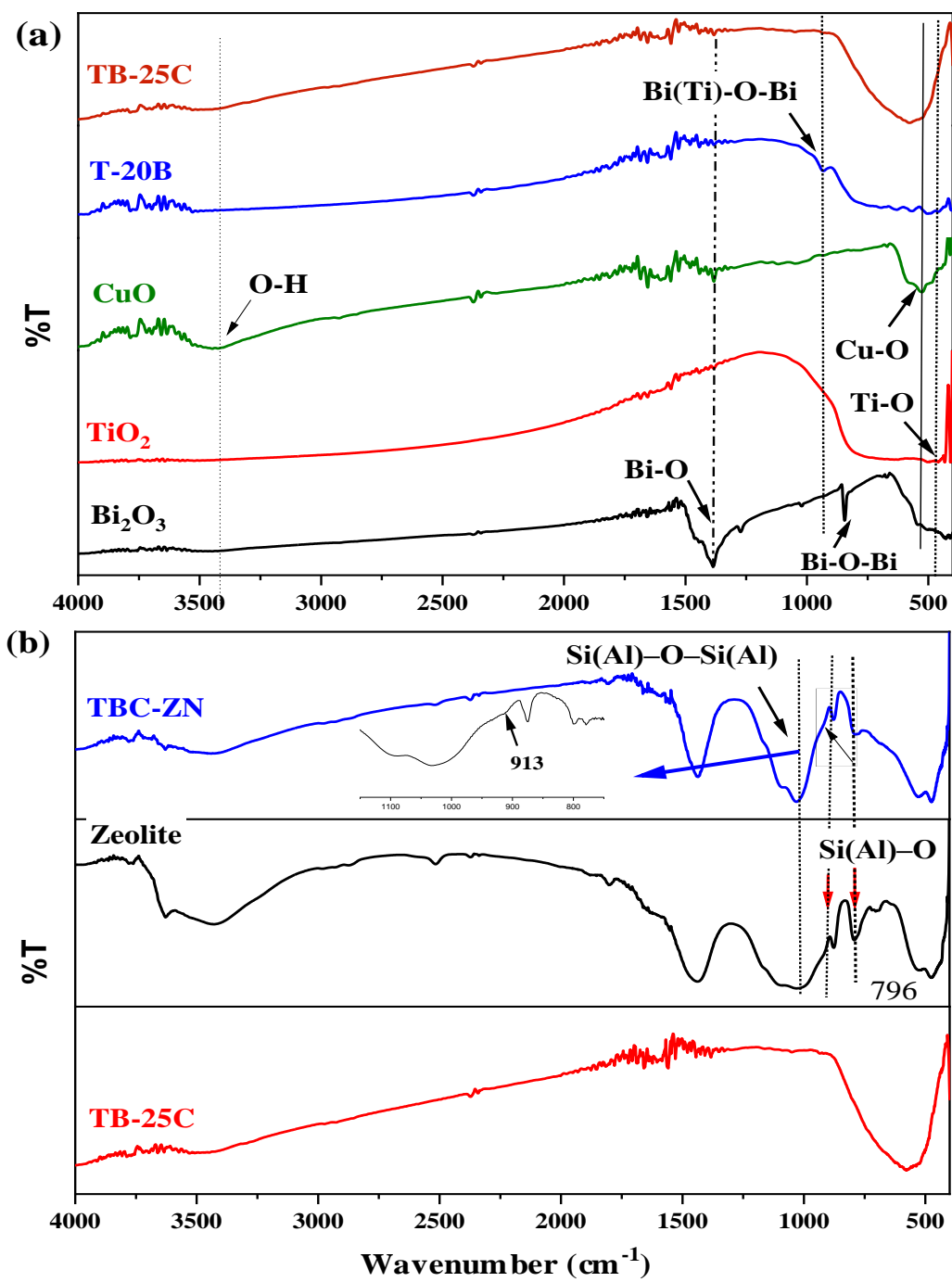
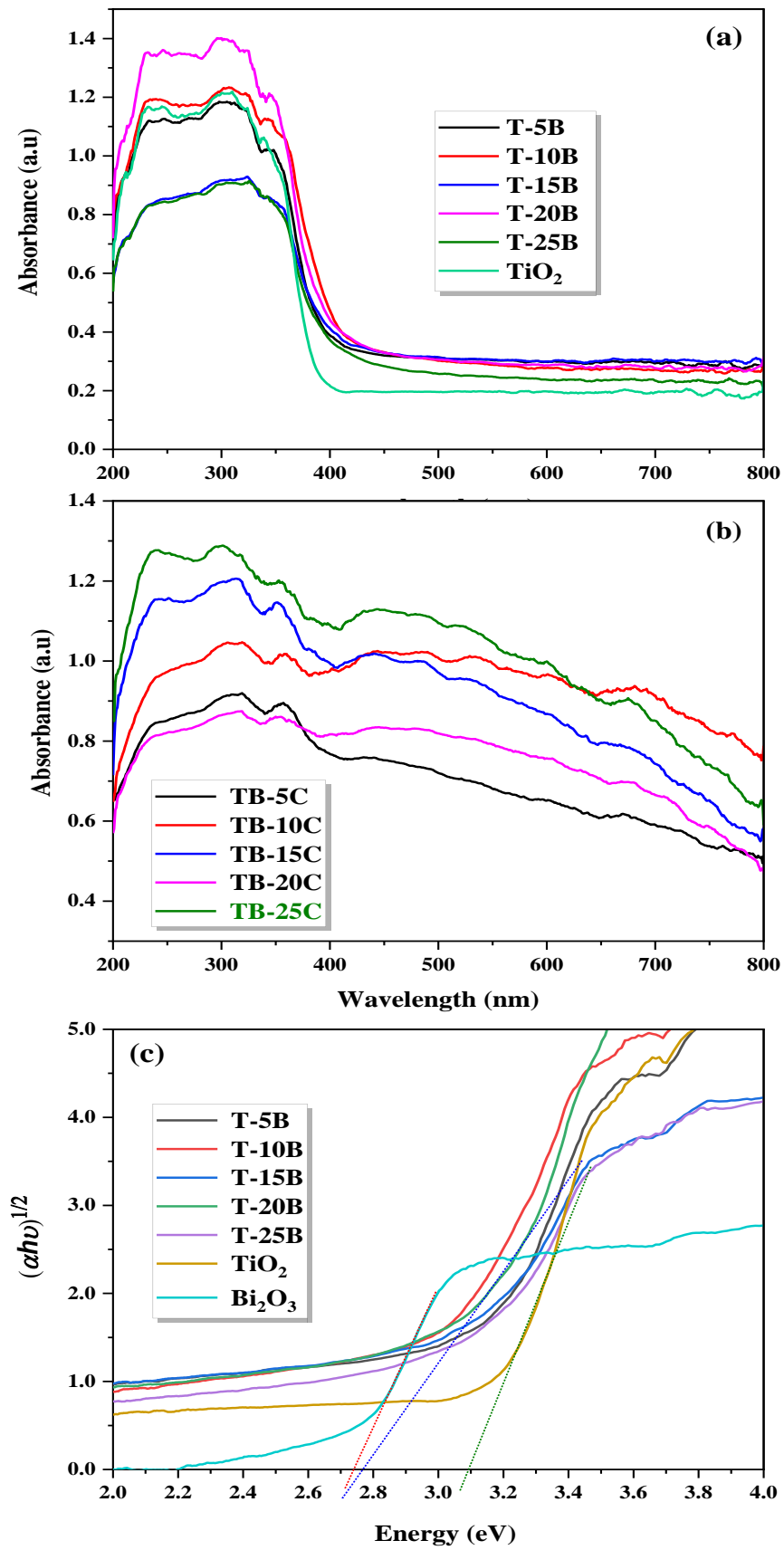
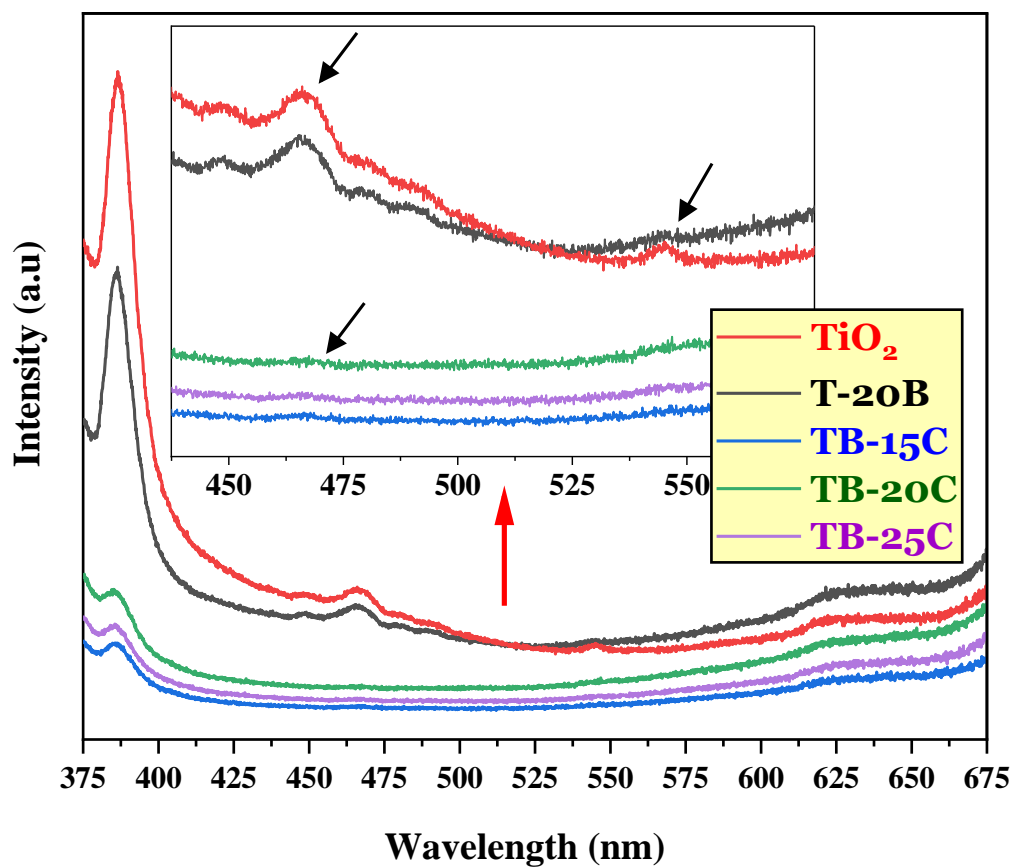


Figure 3. FT-IR spectra of TB<sub>x</sub>C<sub>y</sub> and TBC-ZN



**Figure 4.** (a)–(b) UV–visible spectra and (c) Tauc relation plots of the prepared materials



**Figure 5.** Photoluminescence spectra of different composite.



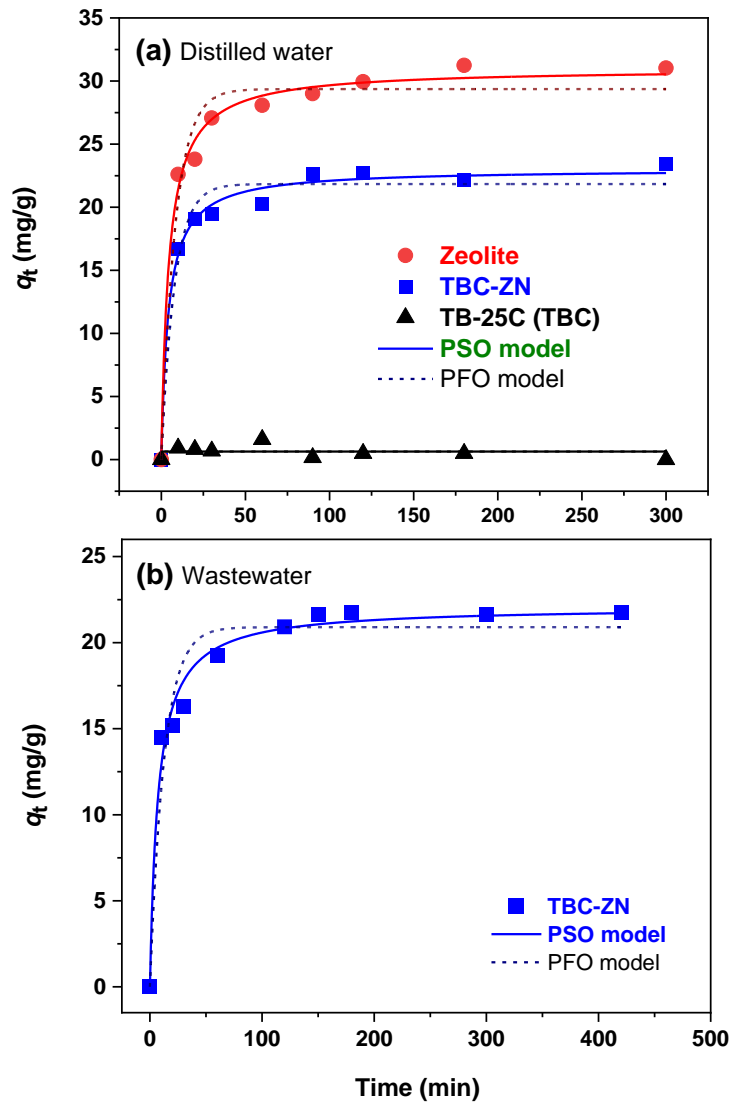


**Figure 6.** Adsorption kinetics of SO dye prepared in (a) distilled water (b) wastewater

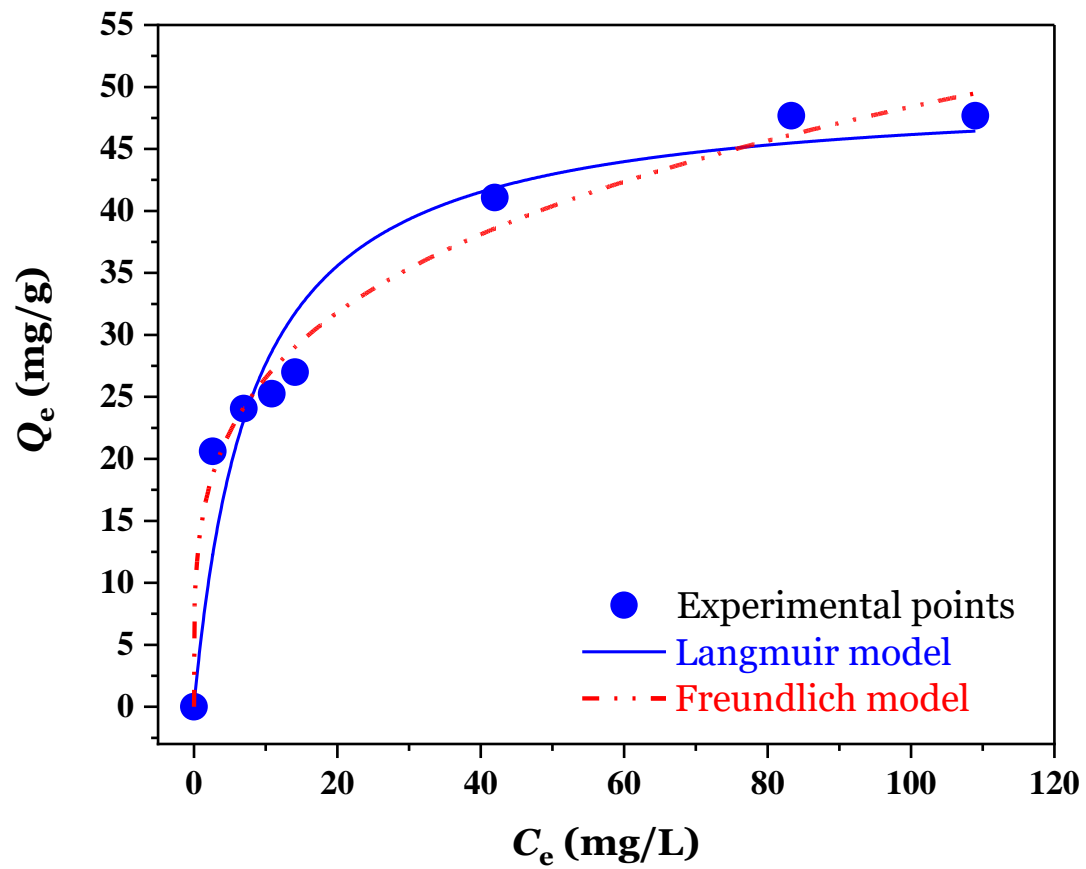


**Figure 7.** Langmuir and Freundlich adsorption isotherms models for SO adsorption on TBC-ZN

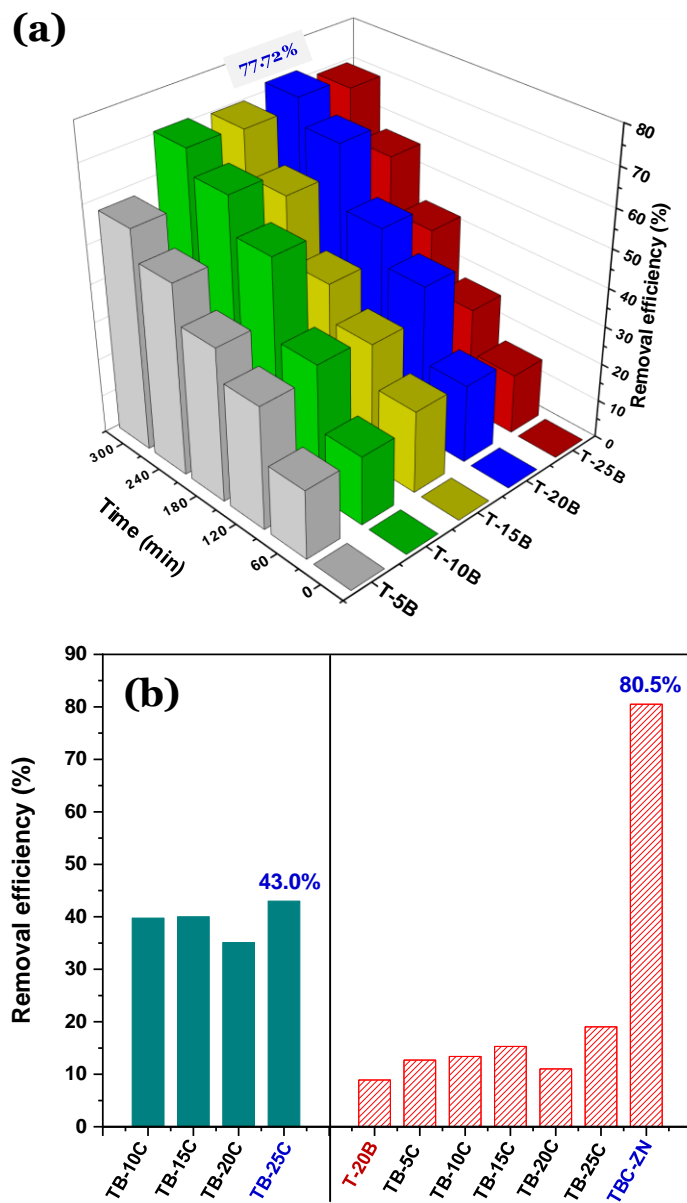


**Figure 8.** a) Photocatalytic activity of binary solution under visible light, b) Photocatalytic activity of ternary solution and TB-25C supported on the raw zeolite under sunlight with  $m/V = 0.4$  g/L and  $C_0$  of dye = 20 mg/L

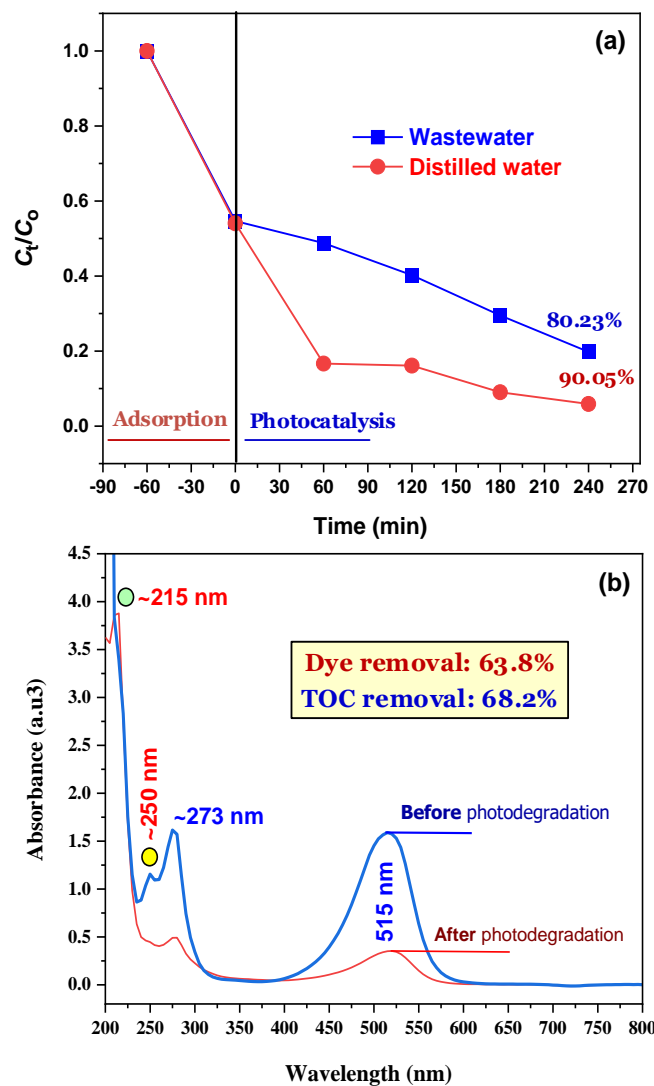


**Figure 9.** (a) Effective removal of SO dye (prepared in distilled water and wastewater) by TBC-ZN by adsorption and photocatalysis processes and (b) UV–VIS absorption spectrum of SO dye in wastewater before and after photocatalysis

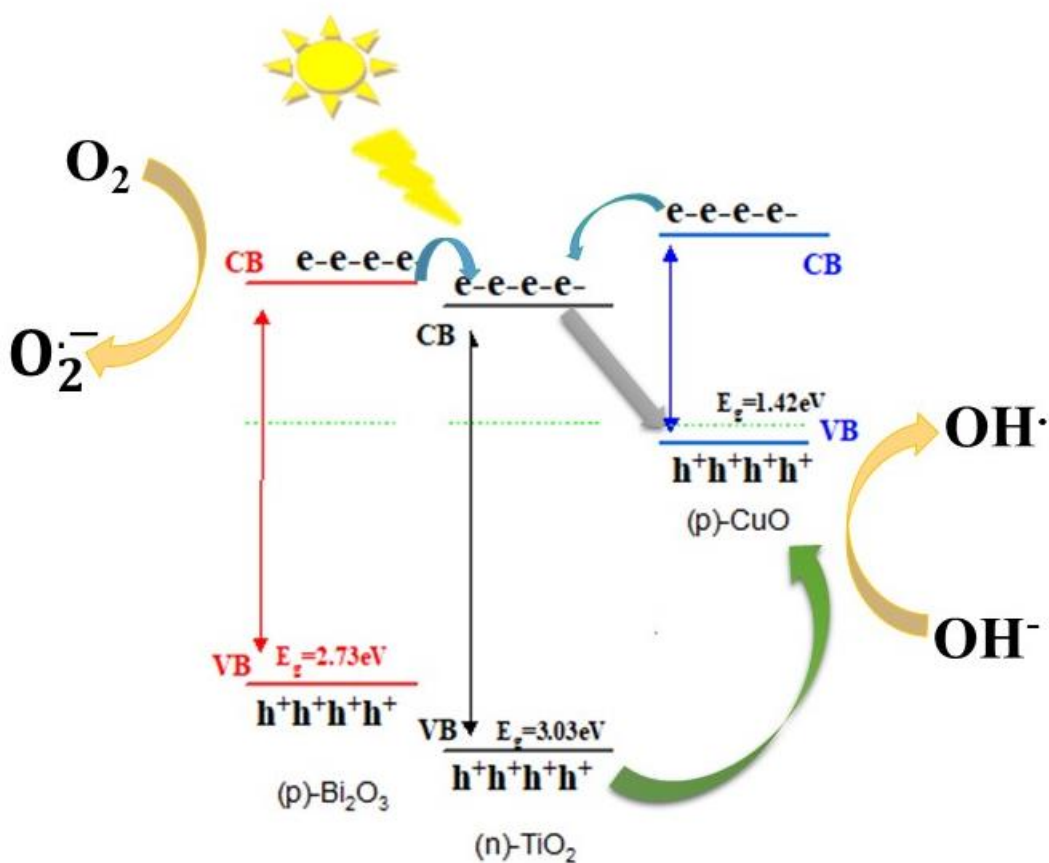
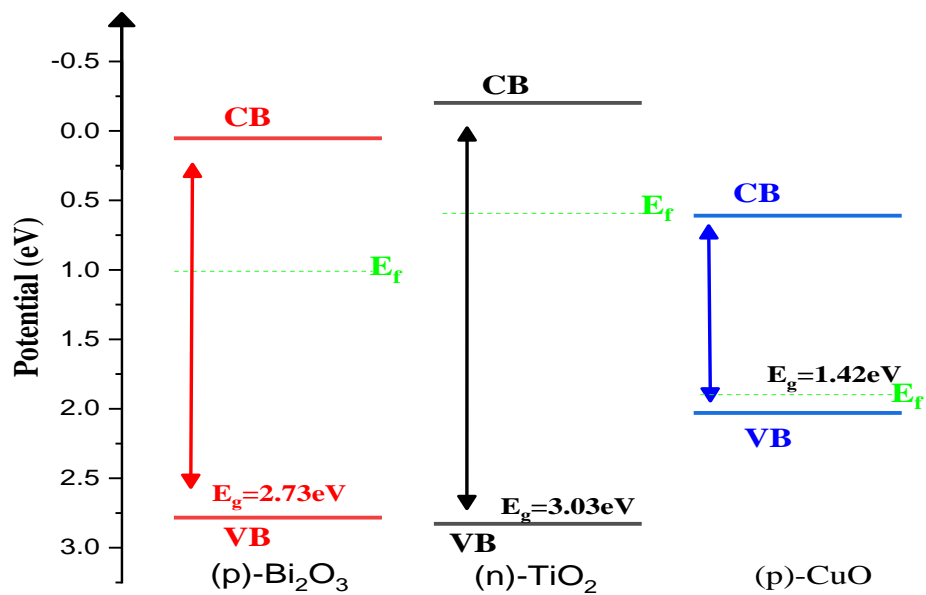


**Figure 10. a)** Energy band diagram of the  $\text{TiO}_2$ ,  $\text{Bi}_2\text{O}_3$  and  $\text{CuO}$  before the contact; b) Energy band diagram of the TBC heterojunction.

## **List of tables**

**Table 1.** Optical properties of binary and ternary solutions

**Table 2.** Kinetics parameters for adsorbing SO dye under different conditions (dye was dissolved in distilled water and real wastewater)

**Table 3.** Parameters of the Langmuir and Freundlich isotherm models for adsorbing SO dye by TBC-ZN

**Table 4.** Kinetics result for the pseudo-first kinetics model for the degradation of SO dye solutions prepared in distilled water and wastewater using TBC-ZN

**Table 1.** Optical properties of binary and ternary solutions

Compound	Band gap (eV)	Wavelength of light required for photoactivation (nm)
TiO <sub>2</sub>	3.03	409.2
Bi <sub>2</sub> O <sub>3</sub>	2.73	454.2
T-5B	2.96	418.9
T-10B	2.75	450.9
T-15B	2.73	454.2
T-20B	2.72	455.9
T-25B	2.78	446.0
TB-5C	2.14	579.4
TB-10C	1.91	642.5
TB-15C	1.80	500.0
TB-20C	1.73	716.8
TB-25C	1.66	747.0

**Table 2.** Kinetics parameters for adsorbing SO dye under different conditions (dye was dissolved in distilled water and real wastewater)

	$q_{e(\text{exp})}$	PFO model				PSO model			
		$q_{e(\text{PFO})}$	$k_1$	adj- $R^2$	red- $\chi^2$	$q_{e(\text{PSO})}$	$k_2$	adj- $R^2$	red- $\chi^2$
<b>1. Distilled water condition</b>									
Zeolite	30.31	29.36	0.119	0.9651	3.325	30.99	0.0072	0.9912	0.834
TBC-ZN	22.76	21.84	0.126	0.9673	1.725	23.03	0.0103	0.9902	0.517
TB-25C (TBC)	0.381	0.646	130.4	0.0610	0.244	0.6463	1.3E+45	0.0610	0.244
<b>2. Wastewater condition</b>									
TBC-ZN	22.71	20.90	0.079	0.9363	2.884	22.09	0.0062	0.9810	0.859

**Note:** the unit of  $q_e$  (mg/g),  $k_1$  (/min), and  $k_2$  [g/(mg×min)]

**Table 3.** Parameters of the Langmuir and Freundlich isotherm models for adsorbing SO dye by TBC-ZN

	Unit	Value	Standard error
<b>1. Langmuir model</b>			
$Q_{\max}$	mg/g	49.87	3.660
$K_L$	L/mg	0.1243	0.03463
$R^2$	—	0.9378	—
adj- $R^2$	—	0.9275	—
red- $\chi^2$	—	18.62	—
<b>2. Freundlich model</b>			
$K_F$	(mg/g)/(mg/L) <sup>n</sup>	14.55	1.099
$n$	—	3.832	0.2883
$R^2$	—	0.9872	—
adj- $R^2$	—	0.9850	—
red- $\chi^2$	—	3.843	—

**Table 4.** Kinetics result for the pseudo-first kinetics model for the degradation of SO dye solutions prepared in distilled water and wastewater using TBC-ZN

Water matrix	$k_1$ (1/min)	$C_0$ (mg/L)	Photodegradation (%)
Wastewater	0.0050	11.4	63.83
Distilled water	0.0062	10.6	89.07



# Optical and photocatalytic properties of $\text{TiO}_2\text{-Bi}_2\text{O}_3\text{-CuO}$ supported on natural zeolite for removing Safranin-O dye from water and wastewater

Reguia Boudraa <sup>1</sup>, Djahida Talantikite-Touati <sup>2</sup>, Abdelhafid Souici <sup>3</sup>, Atmane Djermoune <sup>4</sup>, Amira Saidani <sup>5</sup>, Karim Fendi <sup>5</sup>, Abdeltif Amrane <sup>6</sup>, Jean-Claude Bollinger <sup>7</sup>, Hai Nguyen Tran <sup>8,9</sup>, Amina Hadadi <sup>10</sup> Lotfi Mouni <sup>10,\*</sup>

<sup>1</sup> Laboratory of Materials and Durable Development (M2D), University Bouira, 1000, Bouira, Algeria

<sup>2</sup> Laboratoire de Génie de l'Environnement, Faculté de Technologie, Université de Bejaia, 06000 Bejaia, Algérie

<sup>3</sup> Laboratoire de physico-chimie des matériaux et catalyse, Faculté des Sciences Exactes Université de Bejaia, Bejaia 06000, Algeria

<sup>4</sup> Centre de Recherche Scientifique et Technique en Analyses Physico-chimiques (CRAPC), Bou-Ismaïl 42004, Tipaza, Algeria

<sup>5</sup> Laboratory Processes for Materials, Energy, Water and Environment. Faculty of Science and Technology, University of Bouira, 10000 Bouira, Algeria

<sup>6</sup> Université de Rennes, Ecole Nationale Supérieure de Chimie de Rennes, CNRS, ISCR – UMR6226, 35000 Rennes, France

<sup>7</sup> Laboratoire E2Lim (Eau Environnement Limoges), Université de Limoges, 123 Avenue Albert Thomas, 87060 Limoges, France

<sup>8</sup> Center for Energy and Environmental Materials, Institute of Fundamental and Applied Sciences, Duy Tan University, Ho Chi Minh, 700000, Vietnam

<sup>9</sup> Faculty of Environmental and Chemical Engineering, Duy Tan University, Da Nang, 550000, Vietnam

<sup>10</sup> Laboratoire de Gestion et Valorisation des Ressources Naturelles et Assurance Qualité. Faculté SNVST, Université , Bouira 10000, Algeria

\*Corresponding author: E-mail: [l.mouni@univ-bouira.dz](mailto:l.mouni@univ-bouira.dz), Tel.: +213-784-42-62-28

## List of Figures

**Figure S1.** Schematic of the experimental steps: (A) Elaboration of  $(1-x-y)\text{TiO}_2\text{-xBi}_2\text{O}_3\text{-yCuO}$ , (B) Preparation of composite TBC-ZN.

**Figure S2.** EDX spectra of TBC and zeolite before and after acid treatment

**Figure S3.** BET plot of the materials obtained based on the nitrogen adsorption/desorption isotherm at 77 K.

**Figure S4.** Effect of the adsorbent's mass (TBC-ZN) on its adsorption capacities of SO dye

A)-  $(1-x-y)\text{TiO}_2\text{-xBi}_2\text{O}_3\text{-yCuO}$



B)- TB-25C supported on raw zeolite

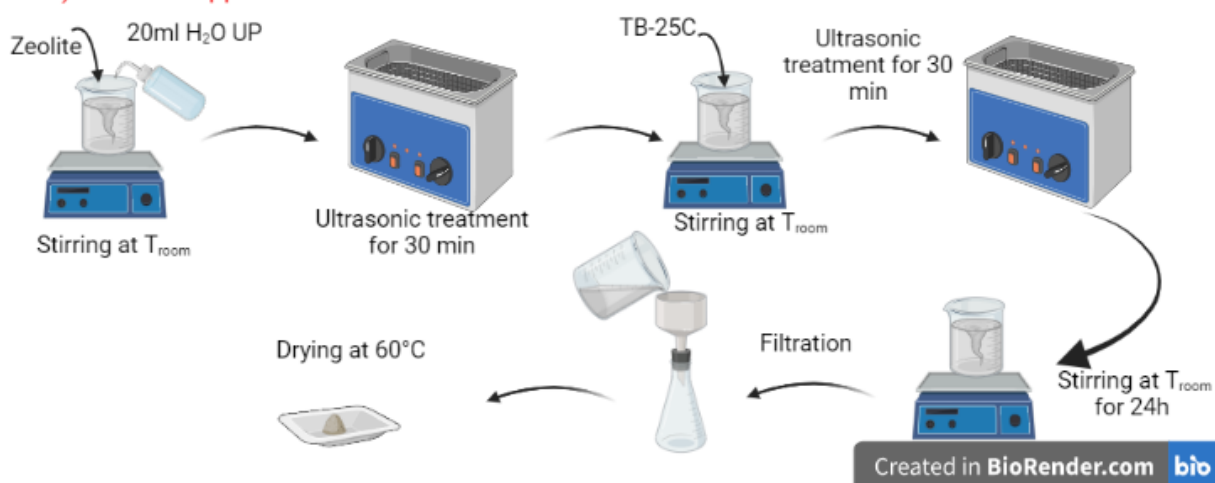


**Figure S1.** Schematic of the experimental steps: (A) Elaboration of  $(1-x-y)\text{TiO}_2\text{-xBi}_2\text{O}_3\text{-yCuO}$ , (B) Preparation of composite TBC-ZN.

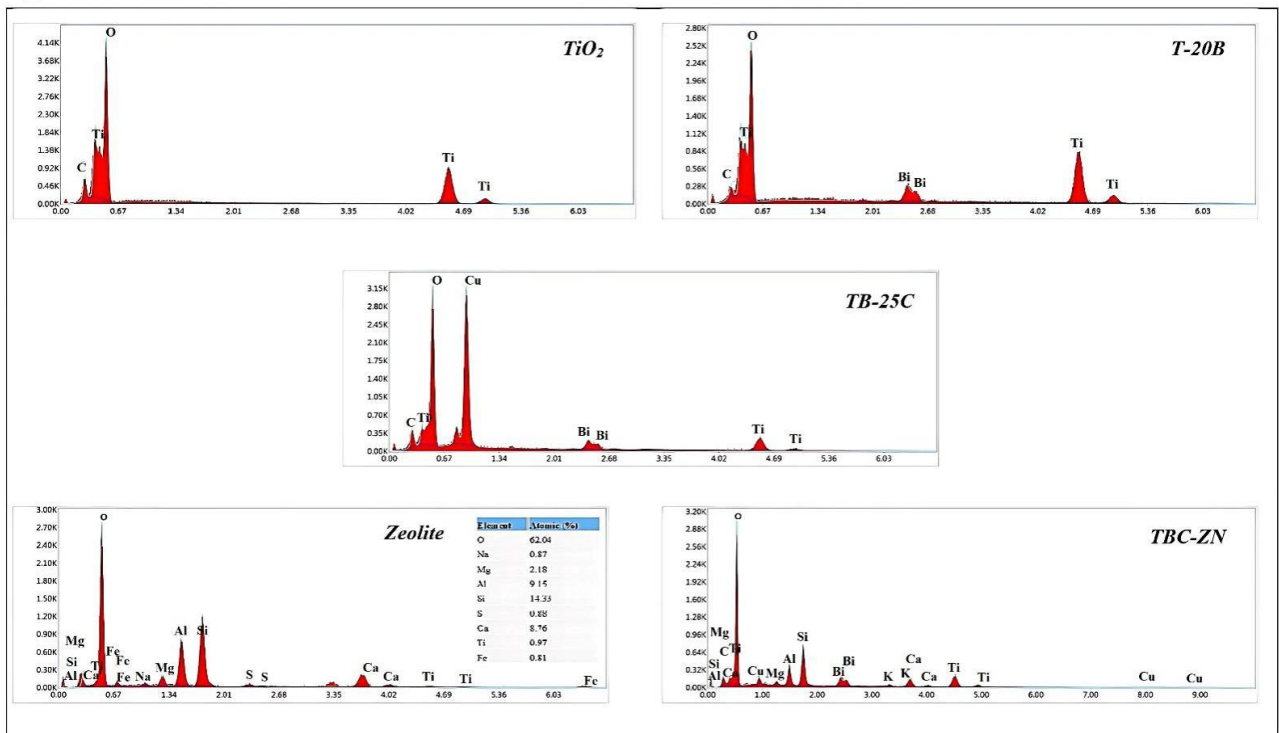


**Figure S2.** EDX spectra of TBC and zeolite before and after acid treatment

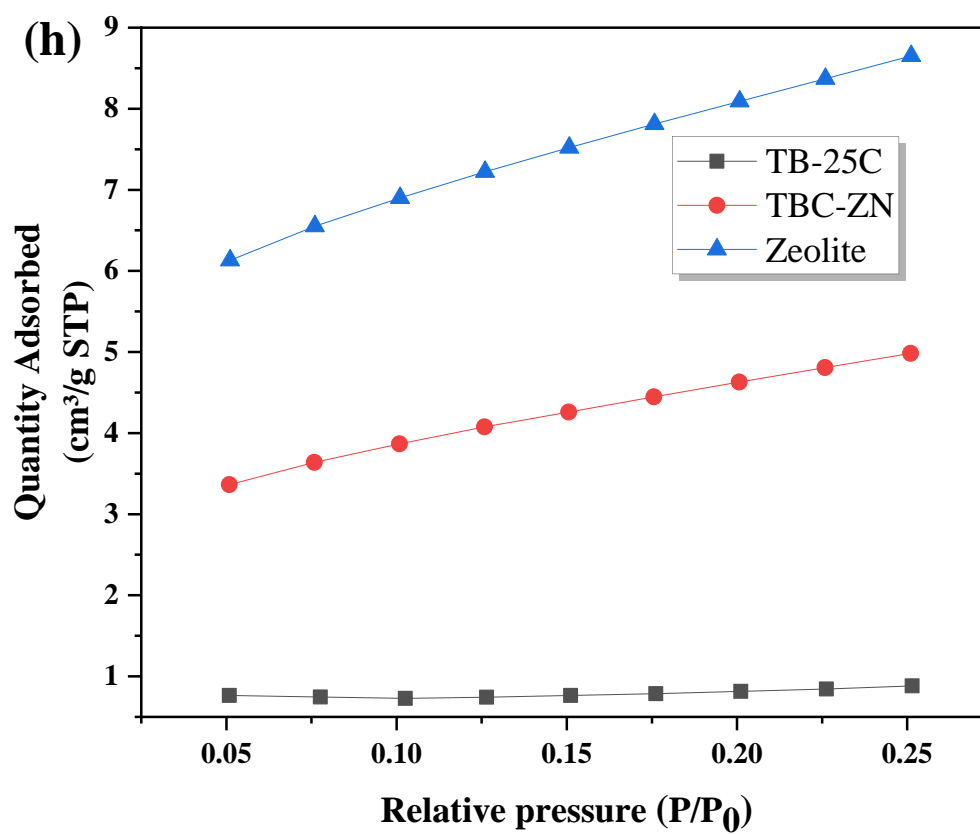


**Figure S3.** BET plot of the materials obtained based on the nitrogen adsorption/desorption isotherm at 77 K.

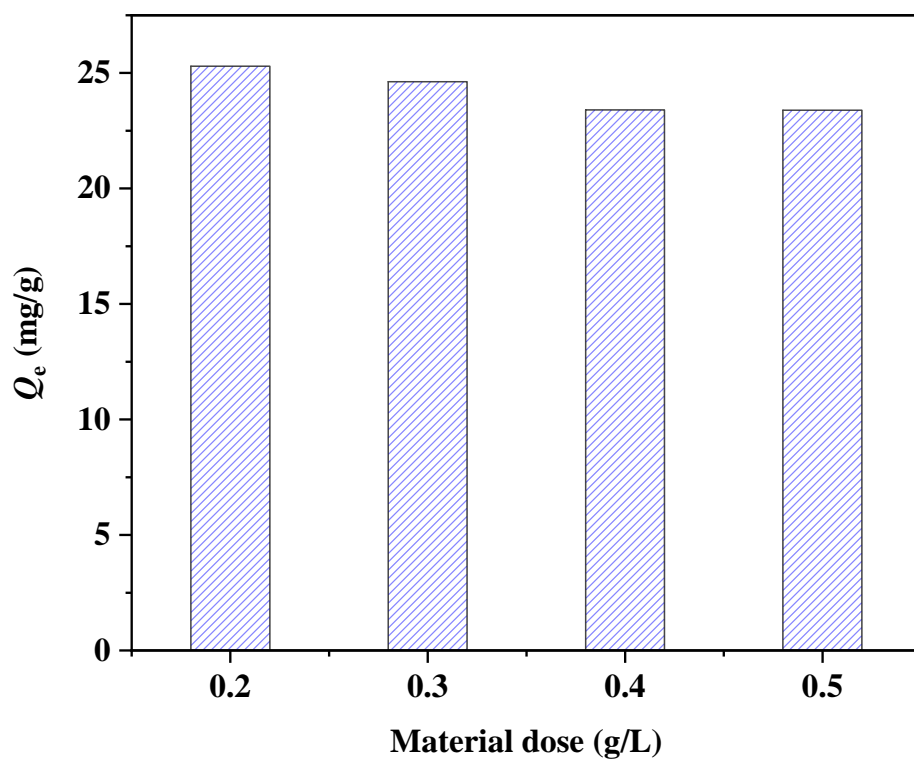


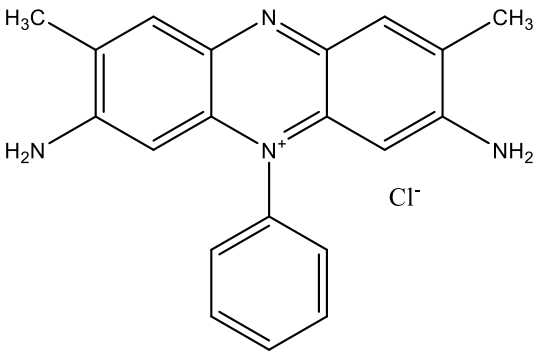
**Figure S4.** Effect of the adsorbent's mass (TBC-ZN) on its adsorption capacities of SO dye

**Table S1.** Characteristics of Safranin O.

**Table S2.** Basic properties of real wastewater.

**Table S3.** Absolute electronegativity, gap energy, calculated CB edge and VB for TiO<sub>2</sub>, Bi<sub>2</sub>O<sub>3</sub> and CuO semi-conductors.

**Table S1.** Characteristics of Safranin-O dye

Properties	Safranin-O dye
Structure	
Chemical formula	$C_{20}H_{19}ClN$
Molecular weight (g/mol)	350.84
Nature	Cationic
$\lambda_{\text{mx}}$	520–525 nm



**Table S2.** Basic properties of real wastewater

<b>Analysis</b>	<b>Results</b>
pH	8.40
Temperature	18 °C
suspended matter	15 mg/L
D.B.O <sub>5</sub>	2.08 mg/L O <sub>2</sub>
D.C.O	9.04 mg/L O <sub>2</sub>
Decantable matter	22 mg/L

**Table S3.** Absolute electronegativity, gap energy, calculated CB edge and VB for TiO<sub>2</sub>, Bi<sub>2</sub>O<sub>3</sub> and CuO semi-conductors.

Materials	absolute electronegativity $X$ (eV)	energy band gap $E_g$ (eV)	calculated CB edge (eV)	calculated VB edge (eV)
TiO <sub>2</sub>	5.813	3.03	-0.202	2.828
Bi <sub>2</sub> O <sub>3</sub>	5.918	2.73	0.053	2.783
CuO	5.82	1.42	0.61	2.01